INTERNATIONAL JOURNAL FOR NUMERICAL METHODS IN FLUIDS
Int. J. Numer. Meth. Fluids 2010; **62**:591–631
Published online 9 March 2009 in Wiley InterScience (www.interscience.wiley.com). DOI: 10.1002/fld.2033

Numerical simulation of a single bubble by compressible two-phase fluids

Siegfried Müller[1,*,†], Philippe Helluy[2] and Josef Ballmann[3]

[1]*Institut für Geometrie und Praktische Mathematik, RWTH Aachen, 52056 Aachen, Germany*
[2]*IRMA, 7 rue Rene-Descartes, 67084 Strasbourg Cedex, France*
[3]*Lehr- und Forschungsgebiet für Mechanik, RWTH Aachen, 52064 Aachen, Germany*

SUMMARY

The present work deals with the numerical investigation of a collapsing bubble in a liquid–gas fluid, which is modeled as a single compressible medium. The medium is characterized by the stiffened gas law using different material parameters for the two phases. For the discretization of the stiffened gas model, the approach of Saurel and Abgrall is employed where the flow equations, here the Euler equations, for the conserved quantities are approximated by a finite volume scheme, and an upwind discretization is used for the non-conservative transport equations of the pressure law coefficients. The original first-order discretization is extended to higher order applying second-order ENO reconstruction to the primitive variables. The derivation of the non-conservative upwind discretization for the phase indicator, here the gas fraction, is presented for arbitrary unstructured grids. The efficiency of the numerical scheme is significantly improved by employing local grid adaptation. For this purpose, multiscale-based grid adaptation is used in combination with a multilevel time stepping strategy to avoid small time steps for coarse cells. The resulting numerical scheme is then applied to the numerical investigation of the 2-D axisymmetric collapse of a gas bubble in a free flow field and near to a rigid wall. The numerical investigation predicts physical features such as bubble collapse, bubble splitting and the formation of a liquid jet that can be observed in experiments with laser-induced cavitation bubbles. Opposite to the experiments, the computations reveal insight to the state inside the bubble clearly indicating that these features are caused by the acceleration of the gas due to shock wave focusing and reflection as well as wave interaction processes. While incompressible models have been used to provide useful predictions on the change of the bubble shape of a collapsing bubble near a solid boundary, we wish to study the effects of shock wave emissions into the ambient liquid on the bubble collapse, a phenomenon that may not be captured using an incompressible fluid model. Copyright © 2009 John Wiley & Sons, Ltd.

Received 11 May 2007; Revised 15 January 2009; Accepted 6 February 2009

KEY WORDS: compressible two-phase flow; stiffened gas; multiscale-based grid adaptation; bubble collapse; bubble solid wall interference; finite volume schemes

*Correspondence to: Siegfried Müller, Institut für Geometrie und Praktische Mathematik, RWTH Aachen, 52056 Aachen, Germany.
†E-mail: mueller@igpm.rwth-aachen.de

Contract/grant sponsor: German Research Foundation (DFG); contract/grant number: MU 1422/4-2

1. INTRODUCTION

The investigation of two-phase flows with bubbles is of special interest in different real-world applications arising, for instance, in engineering [1–3], medical applications [4, 5] and biology [5–7]. The processes taking place in the interior and exterior of a collapsing and oscillating bubble are still subject of theoretical and experimental research, cf. [8]. However, small time and space scales as well as the complicated dynamics make any theoretical and experimental approach a challenge. Therefore, advanced numerical methods are needed to provide simulations that reveal further information about the highly unsteady flow dynamics in the fluid.

The numerical simulation of multi-dimensional compressible two-phase fluid flows still exhibits severe difficulties, in particular, when *strong* differences in the material parameters are present at the phase boundary. Although several models and discretizations have been developed in the past, this can still be considered a challenge.

Previous work on compressible two-phase fluids usually was performed for gas-filled bubbles in a gaseous environment, cf. [9]. If the bubble is surrounded by a liquid, then frequently problems with limited differences of the material parameters are discussed, cf. [10]. The main purpose of the present work is to verify that by the stiffened gas approach of Saurel and Abgrall [11] (i) numerical simulations of *multi-dimensional compressible* two-phase fluids can be performed for *small bubbles* and *realistic* states and (ii) physical features observed in the context with experimental bubble research, cf. [12–14], can be predicted. For this purpose, the stiffened gas approach has to be embedded into an adaptive higher-order discretization. In the following we will give an overview of existing mathematical models and numerical methods and their shortcomings.

Mathematical models: Here we will focus on the modeling and numerical simulation of the collapse of a single gas bubble in a non-stationary, inviscid compressible two-phase flow. In the case of spherical symmetry, this has been studied for an inert gas bubble in compressible liquid by Westenberger [15]. There the Euler equations for inviscid compressible liquids (Tait's equation of state) and a homogenized bubbly fluid, respectively, have been considered. Investigations verified that the fluid thermodynamic state inside the bubble does not stay homogeneous during the collapse. Moreover, shock waves develop and propagate into the ambient liquid preferably just before the bubble reaches its minimum volume. While incompressible models, e.g. the Rayleigh–Plesset equation, have been used to provide useful predictions on the change of a collapsing bubble near a solid boundary [16, 17], the effects of shock wave emissions into the ambient liquid on the bubble collapse may not be captured using an incompressible fluid model. In order to validate the extreme states that may occur due to focusing effects in the liquid as well as in the gas, an explicit finite volume method for the spherical bubble collapse has been developed based on the Navier–Stokes equations using different equations of thermodynamic change of state, e.g. van der Waals and others, [18, 19]. It could be verified that the modeling of the thermodynamic state in the bubble by a perfect gas is only valid for moderate changes in volume.

The numerical simulation of two-phase immiscible flows in compressible fluids is distinguished in the literature between the Lagrangian and the Eulerian approach. In the Lagrangian framework, the interface is typically tracked during the time evolution. There are mainly three types of techniques: (i) particle methods, e.g. Smooth Particle Hydrodynamics, where the movement of particles is simulated, cf. [20, 21], (ii) front tracking methods, where the underlying discretization undergoes a deformation due to the movement of the interface, cf. [22–25], and (iii) Marker methods, e.g. Marker and Cells [26], volume-of-fluid [27], where the discretization is fixed. Typically difficulties arise if the interface changes topologically or becomes complicated. To overcome this difficulty,

DOI: 10.1002/fld

techniques have been developed based on an Eulerian formulation whereby the interface is captured. To distinguish the two-fluid phases in this formulation, the underlying equations of motion are supplemented with an additional scalar equation approximating the position of the interface, for instance, a color function [28] or a level set function [29, 30]. For incompressible two-phase fluid flow, this has been applied with great success, see [31, 32]. In the case of compressible two-phase flow, difficulties arise at the phase boundary caused by pressure oscillations in the numerical simulation. In order to suppress these pressure oscillations, different approaches have been considered in the literature. Abgrall *et al.* proposed a quasi-conservative formulation [9, 11, 33]. Another approach, the ghost fluid method, has been developed by Fedkiw *et al*. [34, 35]. A modification of their ansatz has been introduced by Abgrall and Karni [9, 36] based on a two-flux method. Recently, Sussman [37] suggested a different strategy for computing growth and collapse of gas bubbles where a level set method is coupled with a volume-of-fluid method. However, the liquid is assumed to be incompressible. These methods turn out to give good results for wave processes in flows of two immiscible compressible gases. For instance, in [38, 39] the two-flux method is successfully applied in combination with a level set method to investigate wave interactions at gas–gas interfaces. However, the aforementioned methods either cannot deal with compressible liquids or they fail for compressible liquid–gas flow when a large jump of the acoustic impedance, e.g. several orders of magnitude, is present across the phase interface. Only recently, the real ghost fluid method [10] has been developed that seems to be useful also for this kind of flow problems. In the Eulerian approach the material interface is captured rather than tracked. Therefore, the two phases undergo a numerical phase transition due to the smearing of the material interface. Since the pressure laws for liquids and gases typically are not valid in the same regime of phase space, the numerical mixture of the phases leads to non-physical values in the numerical phase transition regime. This typically causes a break-down of the computation. Among the aforementioned approaches, the stiffened gas approach of Saurel and Abgrall [11] is capable of dealing with *compressible liquid–gas* flow.

Numerical methods: In addition to an adequate mathematical model, highly efficient numerical algorithms are required that allow for a high resolution of the waves produced by the bubble oscillation and their interaction and provide qualitative and quantitative results on the dynamics of these waves. In recent years, a new adaptive concept for finite volume schemes has been developed based on multiscale techniques. First work in this regard has been published by Harten [40, 41] where by means of a multiscale sequence, the flux evaluation is performed. This results in a hybrid scheme working on a uniform grid. Recently, a fully adaptive concept for multiscale finite volume schemes has been developed and investigated [42, 43]. This new concept turns out to be highly efficient and reliable. By now, the new adaptive multi-resolution concept has been applied with great success to different applications, e.g. 2-D/3-D–steady and unsteady computations of compressible fluids about airfoils modeled by the Euler and Navier–Stokes equations, respectively, on block-structured curvilinear grid patches [44], backward-facing step on 2-D triangulations [45] and simulation of a flame ball modeled by reaction–diffusion equations on 3-D Cartesian grids [46, 47]. These applications have been performed for compressible single-phase fluids. More recently, this concept has been extended to two-phase fluid flow of compressible gases, and applied to the investigation of non-stationary shock–bubble interactions on 2-D Cartesian grids for the Euler equations [38, 39].

Outline: In the present work the focus is on the numerical investigation of a single collapsing gas bubble in a compressible liquid. Here the two-phase fluid is modeled by a single compressible medium. In the numerical analysis, a 2-D model problem in the cross-plane of an infinitely long

DOI: 10.1002/fld

cylindrical bubble with its axis parallel to a wall will be considered. For the two phases, we employ the stiffened gas law with different material parameters for the two phases, see Section 2. In Section 3 the stiffened gas model is discretized by the approach of Saurel and Abgrall [11] where the flow equations for the conserved quantities are approximated by a finite volume scheme and an upwind discretization is used for the non-conservative transport equations of the phase indicator (gas fraction). The efficiency of the resulting scheme is improved by applying *multiscale-based grid adaptation techniques*. Note that the discretization is presented in the *multi-dimensional* case on *arbitrary* grids where we employ a *higher-order reconstruction* for the primitive variables. Owing to the non-stationary behavior of the flow, time integration is performed explicitly. The Courant-Friedrich-Levy (CFL) condition of the highest resolution level is locally relaxed by employing the recent multilevel time stepping strategy, cf. [48–50]. The resulting numerical scheme is then applied to the numerical investigation of the collapse of a single gas bubble, see Section 4. To validate the numerical method we first consider a 1-D shock tube problem. The mathematical model is then validated by the planar, cylindrical bubble collapse. Finally, we investigate the 2-D axisymmetric collapse next to a rigid wall where we are interested in the prediction of physical features that have been observed in the experimental bubble research.

2. MATHEMATICAL MODEL

Compressible fluid flow is characterized in continuum mechanics by the fields of density ϱ, velocity $\mathbf{v}$, internal energy e and pressure p distributions. The balances of mass, momentum and energy for inviscid flow lead to the Euler equations in conservation form

$$\begin{aligned} \varrho_t + \operatorname{div}(\varrho \mathbf{v}) &= 0 \\ (\varrho \mathbf{v})_t + \operatorname{div}(\varrho \mathbf{v} \otimes \mathbf{v} + p\mathbf{I}) &= \mathbf{0} \\ (\varrho E)_t + \operatorname{div}(\varrho \mathbf{v}(E + p/\varrho)) &= 0 \end{aligned} \tag{1}$$

where $E = e + 0.5\mathbf{v}^2$ is the total energy. In order to take into account the two different fluids (a gas and a liquid), we introduce a new unknown φ that we call the fraction of gas. We make the convention that $\varphi = 0$ and $\varphi = 1$ correspond to pure liquid and pure gas, respectively. Because we are interested in very high speed flows and very short observation intervals, we suppose that the phase transition can be neglected so that there is no mass transfer between the two fluids, i.e. the two phases are assumed to be immiscible and the gas is considered to be non-condensable. Thus the fraction satisfies a *homogeneous* transport equation, i.e. its material derivative is vanishing,

$$\varphi_t + \mathbf{v} \cdot \nabla \varphi = 0 \tag{2}$$

Using the mass conservation law, it can be written in an equivalent conservative form

$$(\varrho \varphi)_t + \operatorname{div}(\varrho \varphi \mathbf{v}) = 0 \tag{3}$$

which expresses the mass conservation of the involved fluids.

It should be mentioned that we neglect the influence of gravity and surface tension. Ignoring effects of gravity is justified by the assumption of a small diameter of the bubble. Surface tension may become important when the bubble reaches its minimum size. To give account of neglecting it, we will perform in Section 4.2 a comparison of results achieved with this modeling for a cylindrical

DOI: 10.1002/fld

bubble with results computed using the model of Hanke [19] where surface tension is taken into account. Furthermore we neglect viscosity and heat conduction. This will only affect the states in the instant of shock focusing in the bubble center according to Guderley's similarity solution for spherical compression waves, cf. [51], but it will have little effect on the bubble collapse as was found in [19]. On the other hand, viscosity will be significant for the collapse of large bubbles as has been verified by numerical studies in [52]. For the rebound, it is concluded that thermal effects should also be taken into account.

In order to close the system, we have to provide a pressure law

$$p = p(\varrho, e, \varphi) \tag{4}$$

In this work, we consider a relatively simple pressure law: the stiffened gas pressure law suggested in [33, 53]. It reads

$$p(\varrho, e, \varphi) = (\gamma(\varphi) - 1)\varrho e - \gamma(\varphi)\pi(\varphi) \tag{5}$$

Note that the fraction φ takes only the values 1 or 0 for $t > 0$ provided it holds true at the initial time $t = 0$. Thus, there is no physical mixing in the continuous model and it would be sufficient to provide the values of the pressure law coefficients γ and π for $\varphi = 0$ or $\varphi = 1$. However, the numerical model will introduce artificial mixture zones where $0 < \varphi < 1$. Anyway, with a good numerical approximation, the size of the mixture region will tend to zero with the size of the cells in the mesh. But because of the numerical mixture effects, it is necessary to interpolate γ and π for $0 < \varphi < 1$. An arbitrary choice of interpolation could lead to numerical instabilities studied in many works [33, 54, 55], etc. Saurel and Abgrall [11] suggest that a good choice consists of a linear interpolation of two special quantities β_1 and β_2 defined by

$$\begin{cases} \beta_1 = \dfrac{1}{\gamma - 1} \\ \beta_2 = \dfrac{\gamma\pi}{\gamma - 1} \end{cases} \quad \Leftrightarrow \quad \begin{cases} \gamma = 1 + \dfrac{1}{\beta_1} \\ \pi = \dfrac{\beta_2}{1 + \beta_1} \end{cases} \tag{6}$$

The pressure law in the numerical mixture zone is then constructed as follows. First, γ and π are deduced from measurements in the pure fluids. A possible procedure is explained in [53]. For water and air, the material coefficients for the pure phases are listed in Table I. This gives $\gamma(0)$, $\pi(0)$ for the pure liquid and $\gamma(1)$, $\pi(1)$ for the pure gas. We deduce then from (6) the quantities $\beta_1(0)$, $\beta_2(0)$, $\beta_1(1)$, $\beta_2(1)$, and by a linear interpolation

$$\begin{aligned} \beta_1(\varphi) &= \varphi\beta_1(1) + (1 - \varphi)\beta_1(0) \\ \beta_2(\varphi) &= \varphi\beta_2(1) + (1 - \varphi)\beta_2(0) \end{aligned} \tag{7}$$

The mixture pressure law coefficients $\gamma(\varphi)$ and $\pi(\varphi)$ are then obtained from the reverse relation in (6).

Table I. Material coefficients.

	Units	Liquid (water)	Gas (air)
γ	—	7.15	1.4
π	Pa	$3 \cdot e + 8$	0
c_v	J/kg K	201.1	717.5

DOI: 10.1002/fld

To the stiffened gas pressure law (5) we can associate a temperature scale T. The temperature scale is compatible with thermodynamics if it is possible to find an entropy function s such that

$$T\,\mathrm{d}s = \mathrm{d}e + p\,\mathrm{d}(1/\varrho) \tag{8}$$

Several choices are possible. The simplest corresponds to

$$c_v T = e - \frac{\pi}{\varrho} \tag{9}$$

where the constant c_v is the specific heat at constant volume, cf. [56]. The temperature law has no physical meaning in the artificial mixture region because our mixture pressure law has been selected for numerical reasons and not from physical arguments. Since $\gamma = 1 + \mathscr{R}/c_v$ holds in the pure phases, interpolated values for the heat capacity c_v and the specific gas constant $\mathscr{R}$ in the mixture region are computed by

$$c_v(\varphi) = \frac{c_v(0)\,c_v(1)(\gamma(1)-\gamma(0))}{c_v(0)(\gamma(\varphi)-\gamma(0))+c_v(1)(\gamma(1)-\gamma(\varphi))}$$

$$\mathscr{R}(\varphi) = \frac{c_v(1)\,\mathscr{R}(0)(\gamma(1)-\gamma(\varphi))+c_v(0)\,\mathscr{R}(1)(\gamma(\varphi)-\gamma(0))}{c_v(0)(\gamma(\varphi)-\gamma(0))+c_v(1)(\gamma(1)-\gamma(\varphi))}$$

These interpolated values have no clear physical meaning but will be used for a numerical study of the temperature in the mixture region. They are motivated by Barberon and Helluy [56].

Finally, we remark that instead of (2) we might equivalently solve the evolution equations for the material parameters $\boldsymbol{\beta} = (\beta_1, \beta_2)$, which have vanishing material derivatives as they depend only on φ according to Equation (7)

$$\boldsymbol{\beta}_t + \mathbf{v}\cdot\nabla\boldsymbol{\beta} = \mathbf{0} \tag{10}$$

3. NUMERICAL DISCRETIZATION

The numerical discretization of compressible two-phase fluid flow is a challenge of its own. The naive approach to apply a standard finite volume discretization to the coupled system in conservation form (1) and (3) fails to work because of pressure oscillations at the material interface. Cures have been proposed in recent years [11, 34, 57–59]. They are based on non-conservative schemes and worked successfully for gas–gas interfaces. For liquid–gas interfaces the computations will typically break-down after a few time steps. One typically observes severe pressure oscillations at the phase interface due to the numerical diffusion of the density. For the stiffened gas model, as summarized in Section 2, the approach of Saurel and Abgrall [11] also works robustly for liquid–gas interfaces. The basic idea is to apply a finite volume scheme to the flow equations (1) and to employ an upwind discretization of the non-conservative transport equations for the pressure law coefficients (10). Here we summarize the discretization in the *multi-dimensional* case on *arbitrary* grids where we employ a *higher-order reconstruction* for the conserved variables. The efficiency of the resulting scheme is improved by applying recent *multiscale-based grid adaptation techniques* and a *multilevel time stepping strategy*.

DOI: 10.1002/fld

3.1. Finite volume discretization of conserved variables

The Euler equations (1) are solved approximately by a finite volume method on an adaptive grid fixed in space. For this purpose, the finite fluid domain $\Omega \subset \mathbb{R}^d$ is split into a finite set of subdomains, the cells V_i, such that all V_i are disjoint at each instant of time and that their union gives Ω. Furthermore, let $\mathcal{N}(i)$ be the set of cells that have a common edge with the cell i, and for $j \in \mathcal{N}(i)$ let $\Gamma_{ij} := \partial V_i \cap \partial V_j$ be the interface between the cells i and j and $\mathbf{n}_{ij}$ the outer normal of Γ_{ij} corresponding to cell i. The time interval is discretized by $t^{n+1} = t^n + \Delta t$ assuming a constant time step size. On this particular discretization, the finite volume scheme can be written as

$$\mathbf{u}_i^{n+1} = \mathbf{u}_i^n - \frac{\Delta t}{|V_i|} \sum_{j \in \mathcal{N}(i)} |\Gamma_{ij}| \mathbf{F}(\mathbf{u}_{ij}^n, \mathbf{u}_{ji}^n, \mathbf{n}_{ij}) \tag{11}$$

using an explicit time discretization to compute the approximated cell averages $\mathbf{u}_i^{n+1}$ of the conserved variables $\mathbf{u} = (\varrho, \varrho \mathbf{v}, \varrho E)$ on the new time level. Here the numerical flux function $\mathbf{F}(\mathbf{u}, \mathbf{w}, \mathbf{n})$ is an approximation for the flux

$$\mathbf{f}(\mathbf{u}, \mathbf{n}) := \begin{pmatrix} \varrho \mathbf{v} \\ \varrho \mathbf{v} \otimes \mathbf{v} + p \mathbf{I} \\ \varrho \mathbf{v} (E + p/\varrho) \end{pmatrix} \cdot \mathbf{n} = \begin{pmatrix} \varrho v_n \\ \varrho v_n \mathbf{v} + p \mathbf{n} \\ \varrho v_n (E + p/\varrho) \end{pmatrix} \tag{12}$$

in outer normal direction $\mathbf{n}_{ij}$ on the edge Γ_{ij}. Here $v_n = \mathbf{v} \cdot \mathbf{n}$ is the normal velocity component. The numerical flux is assumed to be *consistent*, i.e.

$$\mathbf{F}(\mathbf{u}, \mathbf{u}, \mathbf{n}) := \mathbf{f}(\mathbf{u}, \mathbf{n}) \tag{13}$$

In (11) $\mathbf{u}_{ij}^n$ and $\mathbf{u}_{ji}^n$ are higher-order reconstructions of the value of flow variable $\mathbf{u}$ in cells i and j either side of the interface Γ_{ij}. This higher-order reconstruction results in $\mathbf{u}_{ij}^{n+1}$ depending on a larger stencil than just its immediate neighbors. Furthermore, the pressure law is applied when computing the numerical flux. Therefore, it also depends on the vector of pressure law coefficients $\boldsymbol{\beta}$ associated with the states $\mathbf{u}_{ij}^n$ and $\mathbf{u}_{ji}^n$.

Since a reasonable numerical method should at least be able to maintain a constant flow field, i.e. if $\mathbf{u}(\mathbf{x}, t) = \mathbf{u}_\infty$ for all $(\mathbf{x}, t)$, we require that the numerical solution fulfills $\mathbf{u}_i^n = \mathbf{u}_\infty$ for all index pairs (i, n), too. From the consistency of the numerical fluxes (13) and the discretizations (11), we then obtain for each cell V_i the geometric consistency condition

$$\sum_{j \in N(i)} |\Gamma_{ij}| \mathbf{n}_{ij} = 0 \tag{14}$$

In order to specify the numerical flux, we have to choose the Riemann solver and the reconstruction method. To avoid pressure oscillations at the material interface Saurel and Abgrall [11] suggested in the 1-D case to use solvers that preserve a moving contact discontinuity. In higher dimensions, we therefore require that the condition

$$\mathbf{v}_i^n = \mathbf{v} = \text{const}, \quad p_i^n = p = \text{const} \implies \mathbf{v}_i^{n+1} = \mathbf{v}, \; p_i^{n+1} = p \tag{15}$$

holds for all cells i in the computational domain, i.e. constant pressure and velocity fields are preserved. Note that this condition characterizes a contact discontinuity only in 1-D. In higher

DOI: 10.1002/fld

dimensions, the scheme does not necessarily preserve the normal velocity if there is a jump in the tangential component of the velocity.

For this purpose, in our computations the Riemann problem at the cell interface is solved exactly by the Riemann solver of Colella and Glaz [60] originally developed for real gases. Here we apply it to stiffened gases for which we modify the implementation of the solver as described in [61].

Furthermore, we use a higher-order reconstruction that is applied component-wise to the primitive variables $(\varrho, \mathbf{v}, p, \boldsymbol{\beta})$. The alternative reconstruction of conserved variables or characteristic variables violates the consistency condition (15) and would cause oscillations at the material interface.

In our computations the underlying discretization is always a hierarchy of Cartesian grids. Therefore, we employ a quasi 1-D second-order Essentially Non-oscillatory (ENO) reconstruction and Taylor expansion according to [62] to improve both the spatial and temporal accuracy. See also [61] for details of the implementation.

3.2. Upwind discretization of non-conservative transport equations for pressure law coefficients

Using (11) the conserved quantities can be evolved in time. In addition, we also have to update the fractions before we can proceed with the next time step. However, discretizing the evolution equations (2) or (3) will lead to oscillations at the material interface and spoils the numerical efficiency and stability of the computation. Therefore, Saurel and Abgrall in [11] suggested using an upwind discretization of the non-conservative transport equations (10) for the vector of pressure law coefficients. This is motivated by the requirement that the scheme has to preserve a contact wave for which the tangential component of the velocity is continuous in the sense of (15). A detailed derivation of the discretization in 1-D can be found in [63]. We now extend this approach to the multi-dimensional case on arbitrary grids. For this purpose, we assume that

$$\mathbf{v}_i^n = \mathbf{v} \quad \text{and} \quad p_i^n = p \tag{16}$$

holds for all cells i. Since the reconstruction is performed on the primitive variables, we obtain

$$p_{ij}^n = p_{ji}^n = p \quad \text{and} \quad \mathbf{v}_{ij}^n = \mathbf{v}_{ji}^n = \mathbf{v} \tag{17}$$

whereas the reconstruction of the density ϱ and the material parameters $\boldsymbol{\beta}$ may jump across the cell interface, i.e. $\varrho_{ij}^n \neq \varrho_{ji}^n$ and $\boldsymbol{\beta}_{ij}^n \neq \boldsymbol{\beta}_{ji}^n$. Then the numerical flux computed by the exact Riemann solver is determined by

$$\mathbf{F}(\mathbf{u}_{ij}^n, \mathbf{u}_{ji}^n, \mathbf{n}_{ij}) = \begin{pmatrix} \overline{\varrho}_{ij}\overline{v}_{n,ij} \\ \overline{\varrho}_{ij}\overline{v}_{n,ij}\mathbf{v} + p\mathbf{n}_{ij} \\ \overline{\varrho}_{ij}\overline{v}_{n,ij}(\overline{E}_{ij} + p/\overline{\varrho}_{ij}) \end{pmatrix} \tag{18}$$

where $\overline{\varrho}_{ij}$, $\overline{v}_{n,ij}$ and $\overline{E}_{ij}$ are the density, normal velocity and total energy computed by the Riemann solver. Since the underlying velocity field is homogeneous

$$\overline{v}_{n,ij} = \mathbf{v} \cdot \mathbf{n}_{ij} \tag{19}$$

holds. The material parameters jump only across the material interface, i.e.

$$\overline{v}_{n,ij}\overline{\boldsymbol{\beta}}_{ij} = \boldsymbol{\beta}_{ij}^n \max(\overline{v}_{n,ij}, 0) + \boldsymbol{\beta}_{ji}^n \min(\overline{v}_{n,ij}, 0) \tag{20}$$

DOI: 10.1002/fld

We now insert the flux from Equation (18) into Equation (11). Then we obtain for the discrete continuity equation

$$\varrho_i^{n+1} = \varrho_i^n - \frac{\Delta t}{|V_i|} \sum_{j \in \mathcal{N}(i)} |\Gamma_{ij}| \overline{\varrho}_{ij} \overline{v}_{n,ij} \tag{21}$$

The discrete momentum equation reads

$$(\varrho \mathbf{v})_i^{n+1} = (\varrho \mathbf{v})_i^n - \frac{\Delta t}{|V_i|} \sum_{j \in \mathcal{N}(i)} |\Gamma_{ij}| (\overline{\varrho}_{ij} \overline{v}_{n,ij} \mathbf{v} + p \mathbf{n}_{ij}) \tag{22}$$

Owing to the geometric consistency condition (14) the pressure term vanishes. In the remaining part of Equation (22) we now apply the assumption (16) and use the discrete continuity equation (21), i.e.

$$\varrho_i^{n+1} \mathbf{v}_i^{n+1} = (\varrho \mathbf{v})_i^{n+1} = \left(\varrho_i^n - \frac{\Delta t}{|V_i|} \sum_{j \in \mathcal{N}(i)} |\Gamma_{ij}| \overline{\varrho}_{ij} \overline{v}_{n,ij} \right) \mathbf{v} = \varrho_i^{n+1} \mathbf{v}$$

and, hence,

$$\mathbf{v}_i^{n+1} = \mathbf{v} \tag{23}$$

Finally, the discrete energy equation reads

$$(\varrho E)_i^{n+1} = (\varrho E)_i^n - \frac{\Delta t}{|V_i|} \sum_{j \in \mathcal{N}(i)} |\Gamma_{ij}| \overline{\varrho}_{ij} \overline{v}_{n,ij} (\overline{E}_{ij} + p / \overline{\varrho}_{ij}) \tag{24}$$

Again, the pressure term vanishes because of the the normal velocity (19) and the geometric consistency condition (14). Since $E = e + 0.5\,\mathbf{v}^2$, the remaining equation can be split into two parts for the internal energy and the kinetic energy. Owing to the discrete continuity equations (21) and (23), the latter cancels out and we obtain

$$(\varrho e)_i^{n+1} = (\varrho e)_i^n - \frac{\Delta t}{|V_i|} \sum_{j \in \mathcal{N}(i)} |\Gamma_{ij}| \overline{\varrho}_{ij} \overline{v}_{n,ij} \overline{e}_{ij} \tag{25}$$

According to the pressure law (5), we can rewrite the internal energy as

$$\varrho e = \frac{1}{\gamma - 1} p + \frac{\gamma \pi}{1 - \gamma} = \beta_1 p + \beta_2$$

and, hence, the discrete energy (25) reads

$$(\beta_1)_i^{n+1} p_i^{n+1} + (\beta_2)_i^{n+1} = (\beta_1)_i^n p_i^n + (\beta_2)_i^n - \frac{\Delta t}{|V_i|} \sum_{j \in \mathcal{N}(i)} |\Gamma_{ij}| \overline{\varrho}_{ij} \overline{v}_{n,ij} ((\overline{\beta}_1)_{ij} \overline{p}_{ij} + (\overline{\beta}_2)_{ij})$$

Together with assumptions (16) and (17) we then conclude that $p_i^{n+1} = p$ holds provided that the pressure law coefficients satisfy the discrete evolution equations

$$\boldsymbol{\beta}_i^{n+1} = \boldsymbol{\beta}_i^n - \frac{\Delta t}{|V_i|} \sum_{j \in \mathcal{N}(i)} |\Gamma_{ij}| \overline{v}_{n,ij} \overline{\boldsymbol{\beta}}_{ij} \tag{26}$$

DOI: 10.1002/fld

These are sufficient but not necessary conditions. Note that (26) is a non-conservative upwind discretization for the evolution equations (10) of the material parameters because $\overline{v}_{n,ij}\overline{\boldsymbol{\beta}}_{ij} \neq -\overline{v}_{n,ji}\overline{\boldsymbol{\beta}}_{ji}$. Furthermore, we remark that (26) coincides with the 1-D discretization in [11, 63]. To see this we rewrite the sum in (26) by means of (14) and (19), (20) as

$$\sum_{j\in\mathcal{N}(i)} |\Gamma_{ij}|\overline{v}_{n,ij}\overline{\boldsymbol{\beta}}_{ij} = \sum_{j\in\mathcal{N}(i)} |\Gamma_{ij}|\overline{v}_{n,ij}(\overline{\boldsymbol{\beta}}_{ij} - \boldsymbol{\beta}_i^n) \tag{27}$$

Finally, we obtain the upwind discretization of the pressure law coefficients

$$\boldsymbol{\beta}_i^{n+1} = \boldsymbol{\beta}_i^n - \frac{\Delta t}{|V_i|} \sum_{j\in\mathcal{N}(i)} |\Gamma_{ij}|\overline{v}_{n,ij}(\overline{\boldsymbol{\beta}}_{ij} - \boldsymbol{\beta}_i^n) \tag{28}$$

where the velocity of the material interface in normal direction $\overline{v}_{n,ij}$ is generally not given by (19), but results from the solution of the respective Riemann problem.

Then the numerical discretization of the two-phase fluid model consists of the following procedures in each time step:

(1) compute the reconstruction of the primitive variables,
(2) solve the Riemann problem for each cell interface,
(3) evolve density, momentum and energy in time by (11) where the numerical fluxes at the cell interfaces are determined by (12) with $\mathbf{u}$ the solution of the Riemann problem,
(4) evolve the pressure law coefficients in time by (28) where the transport velocities at each cell interface are determined by the velocities of the Riemann solution.

Since the transport scheme (26) and (28), respectively, is linear in φ and due to the linear interpolation (7) of $\boldsymbol{\beta}$, it is equivalent to solve the evolution equation for the fraction φ, i.e.

$$\varphi_i^{n+1} = \varphi_i^n - \frac{\Delta t}{|V_i|} \sum_{j\in\mathcal{N}(i)} |\Gamma_{ij}|\overline{v}_{n,ij}\overline{\varphi}_{ij} = \varphi_i^n - \frac{\Delta t}{|V_i|} \sum_{j\in\mathcal{N}(i)} |\Gamma_{ij}|\overline{v}_{n,ij}(\overline{\varphi}_{ij} - \varphi_i^n) \tag{29}$$

3.3. Multiscale-based grid adaptation

The numerical simulation of collapsing bubbles is a high-dynamic process governed by compression and rarefaction waves and their interaction with the material boundary and solid walls, cf. [38]. In order to catch properly all these effects, high resolution discretizations are needed. However, uniform discretizations cannot be afforded due to extremely high computational costs both in terms of CPU time and memory. Therefore, highly efficient schemes are needed that adapt the grid to the flow solution such that a high resolution is only used locally where strong variations in the flow field occur. In order to improve the efficiency of the numerical scheme presented in Sections 3.1 and 3.2, we employ recent multiscale-based grid adaptation techniques, cf. [42, 43]. These have been proven to be very efficient and reliable for many applications, cf. [44]. Here we briefly summarize the basic conceptual ideas. For technical details we refer the reader to [42].

Step 1: *Multiscale analysis*. The fundamental idea is to present the cell averages $\hat{\mathbf{u}}_L$ representing the discretized flow field at fixed time level t^n on a given uniform highest level of resolution $l = L$ (*reference mesh*) associated with a given finite volume discretization (*reference scheme*) as cell averages on some coarsest level $l = 0$ where the fine scale information is encoded in arrays of *detail coefficients* $\mathbf{d}_l$, $l = 0, \ldots, L-1$, of ascending resolution, see Figure 1. For this purpose,

DOI: 10.1002/fld

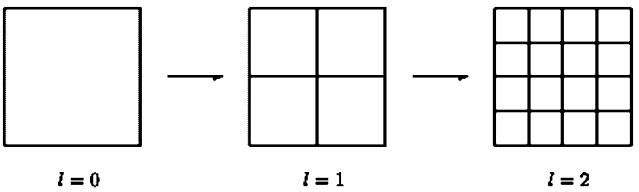

Figure 1. Sequence of nested grids.

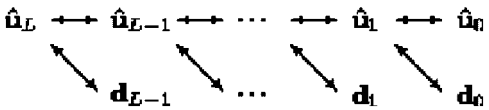

Figure 2. Multiscale transformation.

one might use Harten's discrete concept of reconstruction and prediction, cf. [64], or biorthogonal wavelets, cf. [65].

The multiscale decomposition is performed on a hierarchy of *nested* grids $\mathcal{G}_l$ with increasing resolution $l=0,\ldots,L$, see Figure 2. In our computations presented here we confine attention to structured curvilinear grids though the general framework is not restricted to this configuration, but can also be applied to *unstructured* grids and *irregular* grid refinements in arbitrary space dimensions.

Step 2: *Thresholding*. It can be shown that the detail coefficients become small with increasing refinement level when the underlying function is locally smooth. In order to compress the original data, this motivates us to discard all detail coefficients $d_{l,\lambda}$ whose absolute values fall below a level-dependent threshold value $\varepsilon_l=2^{l-L}\varepsilon$. Let $\mathcal{D}_{L,\varepsilon}$ be the set of *significant details*. The ideal strategy would be to determine the threshold value ε such that the *discretization error* of the reference scheme, i.e. difference between exact solution and reference scheme, and the *perturbation error*, i.e. the difference between the reference scheme and the adaptive scheme, is balanced, see [43].

Step 3: *Prediction and grading*. Since the flow field evolves in time, grid adaptation is performed after each evolution step to provide the adaptive grid at the *new* time level. In order to guarantee the adaptive scheme to be *reliable* in the sense that no significant future feature of the solution is missed, we have to *predict* all significant details at the new time level $n+1$ by means of the details at the *old* time level n. Let $\tilde{\mathcal{D}}_{L,\varepsilon}^{n+1}\supset\mathcal{D}_{L,\varepsilon}^{n}\cup\mathcal{D}_{L,\varepsilon}^{n+1}$ be the prediction set. The prediction strategy is detailed in [43]. In view of the grid adaptation step, this set is additionally inflated such that it corresponds to a graded tree.

Step 4: *Grid adaptation*: By means of the set $\tilde{\mathcal{D}}_{L,\varepsilon}^{n+1}$ a locally refined grid is determined. For this purpose, we recursively check in the preceding level, from coarse to fine, whether there exists a significant detail to a cell. If there is one, then we refine the respective cell. We finally obtain the locally refined grid with hanging nodes represented by the index set $\mathcal{G}_{L,\varepsilon}$. This procedure is graphically sketched in Figure 3. To each shaded cell there is at least one significant detail. These cells are removed and replaced by their children on the next higher level. This results in a grid with hanging nodes.

DOI: 10.1002/fld

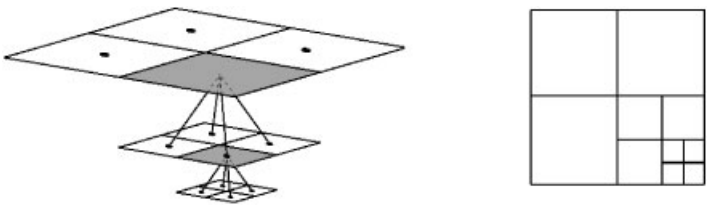

Figure 3. Grid adaptation: refinement tree (left) and corresponding adaptive grid (right).

Since the concept of multiscale-based grid adaptation has been presented and discussed in detail in previous publications, we omit the technical details needed to realize it. However, we comment on some aspects that were not addressed in single-phase computations. Note that the grid adaptation concept has been developed and investigated originally for finite volume schemes. Here the numerical discretization is a hybrid scheme where the conserved variables $\mathbf{u}$ of mass, momentum and energy are discretized by a finite volume scheme (11) and the pressure law coefficients $\boldsymbol{\beta}$ by an upwind discretization (28) in non-conservative form. Nevertheless, we can apply the grid adaptation to the conserved and non-conserved variables although two changes have to be made to account for the extension to two-phase fluid flow and the non-conservative discretization of the pressure law coefficients. These concern the threshold process and the flux computation at hanging nodes.

Threshold process: Since the physical states in liquid and gas differ extremely in scale, it turned out in our computations that we had to modify slightly the threshold process. In previous single-phase computations, cf. [44], the details for each physical quantity were scaled by its maximum in the entire computational domain. This has been useful to adjust the scales of the different quantities; otherwise, different threshold values ε have to be used for different quantities that usually differ by several orders of magnitude. In the present two-phase computations, this turned out to be inadequate. Owing to the huge values in the liquid, the maximum for each quantity is large and scaling by it would make the details corresponding to the gas phase very small and they would be discarded in the threshold process. Hence, waves in the gas phase would not be properly resolved. Therefore, we had to replace the global maximum by a local maximum where only the cells in the stencil of the detail are taken into account.

Flux computation at hanging nodes: Another issue that had to be adjusted concerns the computation of the gradients in (28) at interfaces with hanging nodes. For the numerical fluxes in (11) the strategy was unchanged. First, the numerical fluxes on the higher scale are computed by values on the same refinement level. In case the neighboring cells correspond to higher or lower scales the data are projected to the respective level by means of the multi-scale transformation. Then the numerical flux on the coarser scale is the sum of all fluxes on higher scale by which the coarse interface is composed. This is shown in Figure 4. This procedure is motivated by applying the multiscale decomposition to the evolution equations (11). Then by the conservation property the fluxes corresponding to internal fluxes cancel and only the fine-grid fluxes contribute to the edges of the coarse-grid cells, see Figure 5. Similarly, we proceed with the evolution equations (28). However, due to the non-conservative discretization, the gradients at the internal interfaces do not cancel. Thus, neglecting these terms will introduce some additional error to the threshold error resulting from higher refinement levels. Nevertheless, to add the fine-grid gradients corresponding to a coarse-grid edge gives satisfactory results and the *non-conservation error* does not spoil the overall accuracy of the computation.

DOI: 10.1002/fld

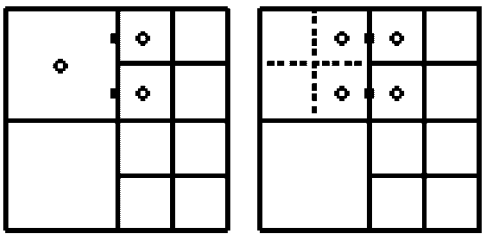

Figure 4. Flux evaluation at interface with hanging node: adaptive grid (left), virtually refined grid (right).

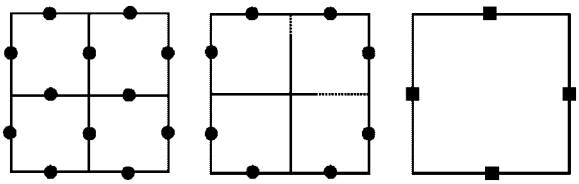

Figure 5. Flux computation: fine grid (left), cancellation due to conservation (middle), coarse grid (right).

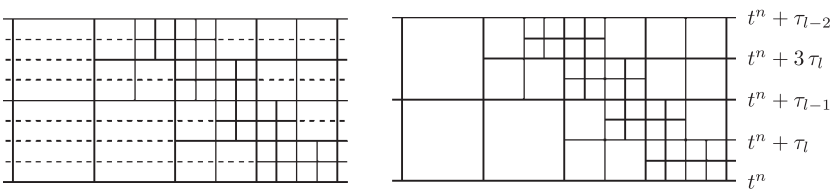

Figure 6. Synchronized time evolution on space–time grid.

3.4. Multilevel time stepping

Since the reference scheme (11) is assumed to use an explicit time discretization, the time step size is bounded due to the CFL condition by the smallest cell in the grid. Hence, Δt is determined by the highest refinement level L, i.e. $\Delta t = \tau_L$. However, for cells on the coarser scales $l = 0, \ldots, L-1$ we may use $\Delta t = \tau_l = 2^{L-l}\tau_L$ to satisfy locally the CFL condition. In [48] a multilevel time stepping strategy has been incorporated recently to the adaptive multiscale finite volume scheme that has been extended to multi-dimensional problems in [49, 50]. Here ideas similar to the predictor–corrector scheme [66] and the Adaptive Mesh Refinement technique [67, 68] are used. The differences between the classical approaches and the multilevel strategy are discussed in detail in [48].

The basic idea is to save flux evaluations where the local CFL condition allows a large time step. The precise time evolution algorithm is schematically described by Figure 6: In a global time stepping, i.e. using $\Delta t = \tau_L$ for all cells, each vertical line section appearing in Figure 6 (left) represents a flux evaluation and each horizontal line (dashed or solid) represents a cell update of $\mathbf{u}$ due to the fluxes. In the multilevel time stepping, a flux evaluation is only performed at vertical line sections that emanate from a point where at least one solid horizontal line section emanates from. If a vertical line section emanates from a point, where two dashed horizontal sections emanate

DOI: 10.1002/fld

from, then we do not recompute the flux, but keep the flux value from the preceding vertical line section. Hence fluxes are only computed for the vertical edges in Figure 6 (right).

Note that on each intermediate time level (horizontal lines) **u** is updated for *all* cells and that grid adaptation is performed at each *even* intermediate time level, i.e. at $t^n + k\tau_L$ for k even. Hence it is possible to track, for instance, a shock movement on the intermediate time levels instead of *a priori* refining the whole range of influence, see Figure 6 (right).

However, the update of **u** for the conserved quantities and the material coefficients makes it necessary to modify the computation of the fluxes corresponding to a coarse cell at grid interface points, i.e. a dashed and a drawn horizontal line emanate from this point. Here the non-conservative fluxes for the material coefficients are not updated to account for the consistency condition (15), whereas the conservative fluxes for the conserved quantities are updated by the new values on the intermediate time level.

4. NUMERICAL RESULTS

We are interested in the numerical investigation of the collapse of a single gas bubble first far away from and second next to a rigid wall, see Figure 7. The mathematical model is based on the stiffened gas approach of Section 2 where the liquid phase is characterized by a stiffened gas law and the gas phase by a perfect gas law, which can both be written in the form (5). The material coefficients for the pure phases are listed in Table I.

The governing equations are the Euler equations (1) and the non-conservative transport equations (10) for the pressure law coefficients. These are discretized by the finite volume scheme (11) and the non-conservative upwind discretization (28). The efficiency of the numerical discretization is significantly improved by the multiscale-based grid adaptation employing multilevel time stepping as summarized in Section 3.3.

Before tackling the aforementioned collapse problems first some important aspects of the numerical modeling are investigated, namely, accuracy, efficiency, reliability and robustness. Then we consider the collapse of a gas-filled cylindrical bubble surrounded by water (2-D) to validate the mathematical model and the collapse of a gas-filled cylindrical bubble next to a rigid wall (2-D)

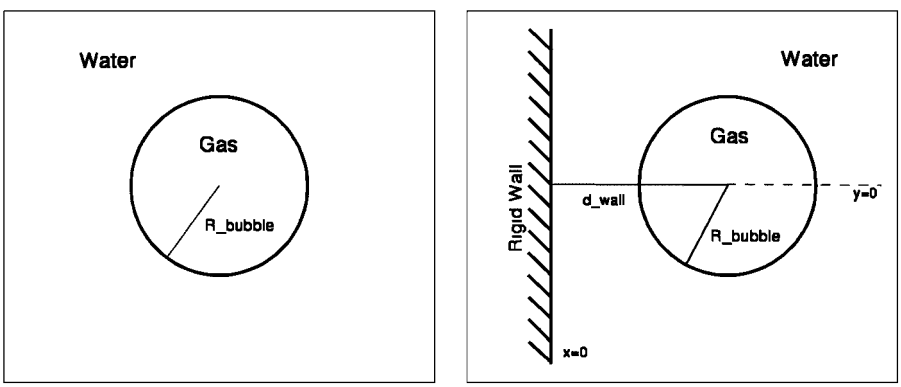

Figure 7. Bubble away (left) and next (right) to a rigid wall.

DOI: 10.1002/fld

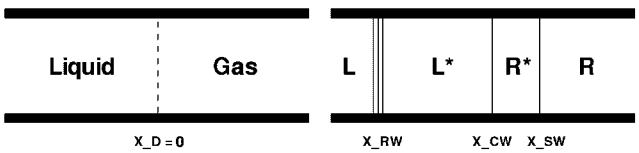

Figure 8. Shock tube problem: initial configuration (left) and solution at some later instant (right).

Table II. Shock tube problem: initial and intermediate states.

		State L	State L*	State R*	State R
	Units	Liquid	Liquid	Gas	Gas
ϱ	kg/m^3	1000	978.672	0.028728	0.026077
v_x	m/s	0	32.998	32.998	0
p	Pa	5e+07	2425.7	2425.7	2118
ϱc	kg/m^2 s	1.58193e+06	1.44889e+06	9.87723	8.79338
τ	m^3/kg	0.001	0.00102179	34.8092	38.348
Ma	—	0	0.022288994	0.095975086	0
T	K	283	247.86	294.2	283

where we are interested in the prediction of physical features that have been observed in the experimental bubble research.

All computations have been performed using the code *QuadConcept* where we employ multiscale-based grid adaptation. This solver is based on the implementation of the adaptive finite volume solver originally developed for compressible single-phase fluids, cf. [42]. It has been extended by the upwind discretization of the pressure law coefficients, see Section 3.2.

4.1. Two-phase Riemann problem

We consider a 1-D shock tube problem in a tube of infinite length where initially two states corresponding to pure liquid (left) and gas (right) are separated by a diaphragm shown in Figure 8 (left).

The initial data corresponding to state L and R taken from [19, p. 41] are listed in Table II. They are characterized by high pressure and density values in the liquid and low pressure and density values in the gas where the temperature is chosen to be in equilibrium. These are, e.g. characteristic for injection nozzles of diesel engines, cf. [69].

On instantaneously removing the membrane a fast expansion wave runs into the liquid phase and a shock wave moves into the gas phase followed by the material interface, see Figure 8 (right). The constant intermediate states are given in Table II. The velocities of the three waves are listed in Table III. We note that the shock speed is only about 25 % of the velocity of the rarefaction wave.

For this simple configuration we performed several computations. The purpose of these computations is twofold, namely, (i) to validate the implementation and the numerical discretization with respect to accuracy, robustness and reliability and (ii) to investigate the effect of higher-order reconstruction, grid adaptation and multilevel time stepping on the numerical results.

DOI: 10.1002/fld

Table III. Shock tube problem: wave speeds.

$v_{RW}^{-}=v_{R-}-c_{R-}$	$v_{RW}^{+}=v_{R+}-c_{R+}$	v_{CW}	v_{SW}
−1581.93	−1447.46	32.998	357.588

The computational domain is $\Omega=[-2, 0.5]$ and the final time is $t=1.001984\times10^{-3}$ s. The coarse grid discretization consists of $N_0=50$ cells. The number of refinement levels is always $L=8$. From this we infer that the (uniform) reference grid on level L is composed of $N_L=12\,800$ cells. We use a fixed time step size $\Delta t=3.1312\times10^{-8}$ s for all time steps. It has been chosen such that the CFL condition holds for CFL number 0.25 with respect to the initial data. Hence, we perform $n=32\,000$ time steps. If not stated, otherwise, the threshold value is $\varepsilon=0.0001$ and we use the second-order reconstruction of the primitive variables ϱ, v and p. The computations are performed employing multilevel time stepping.

Validation: In Figure 9 the numerical results and the exact solution are shown for the final time. The exact solution of the Riemann problem was computed by the iterative solver of Colella and Glaz [60]. We note that the numerical results are in good agreement with the exact solution except for the temperature at the material interface. The problem on the temperature has already been reported in [70].

Nevertheless, there are some deficiencies that become visible only if one zooms into the solution. First consider the solution in the vicinity of the contact discontinuity shown in Figure 10. We observe that the numerical discretization of the pressure law coefficients leads to a smearing of the mass and volume fraction, see Figure 10(d) and (h), though the underlying mathematical model in Section 2 is based on the assumption of immiscibility. This numerical mass diffusion causes an overheating in the liquid and gas phase next to the material interface, see Figure 10(c). In addition, we observe some effect due to the numerical mass diffusion on the Mach number in the gas phase, see Figure 10(g).

Another deficiency can be observed in the liquid phase of Figure 12. In particular, consider the pressure of Figure 12(a). For the second-order accurate scheme, we see an over-expansion of the liquid with pressure falling below the analytical solution. In contrast, with the first-order accurate scheme, the excessive numerical dissipation results in poor resolution of the position of the contact.

Furthermore, we note that the position of the material interface, see Figure 10, and the position of the shock wave, see Figure 11, differ slightly between the numerical results and the exact solution. Most significant is the difference for the specific volume at the material interface displayed in Figure 10(b). This is caused by the non-conservative discretization of the transport equations for the pressure law coefficients. In return, we note that pressure and velocity are constant across the material interface and no oscillations are introduced according to the construction of the upwind discretization (28), see Figure 10(a) and (f).

Although there are some deficiencies, we want to emphasize that these effects are local and can only be observed on very small scales.

Influence of thresholding, time stepping and reconstruction: Next we investigate the influence of the higher-order reconstruction on the numerical results. For this purpose we performed computations using first-order and second-order reconstruction, respectively, and compared these with the exact solution. As we may conclude from Figure 11 the shock wave is much sharper resolved for

DOI: 10.1002/fld

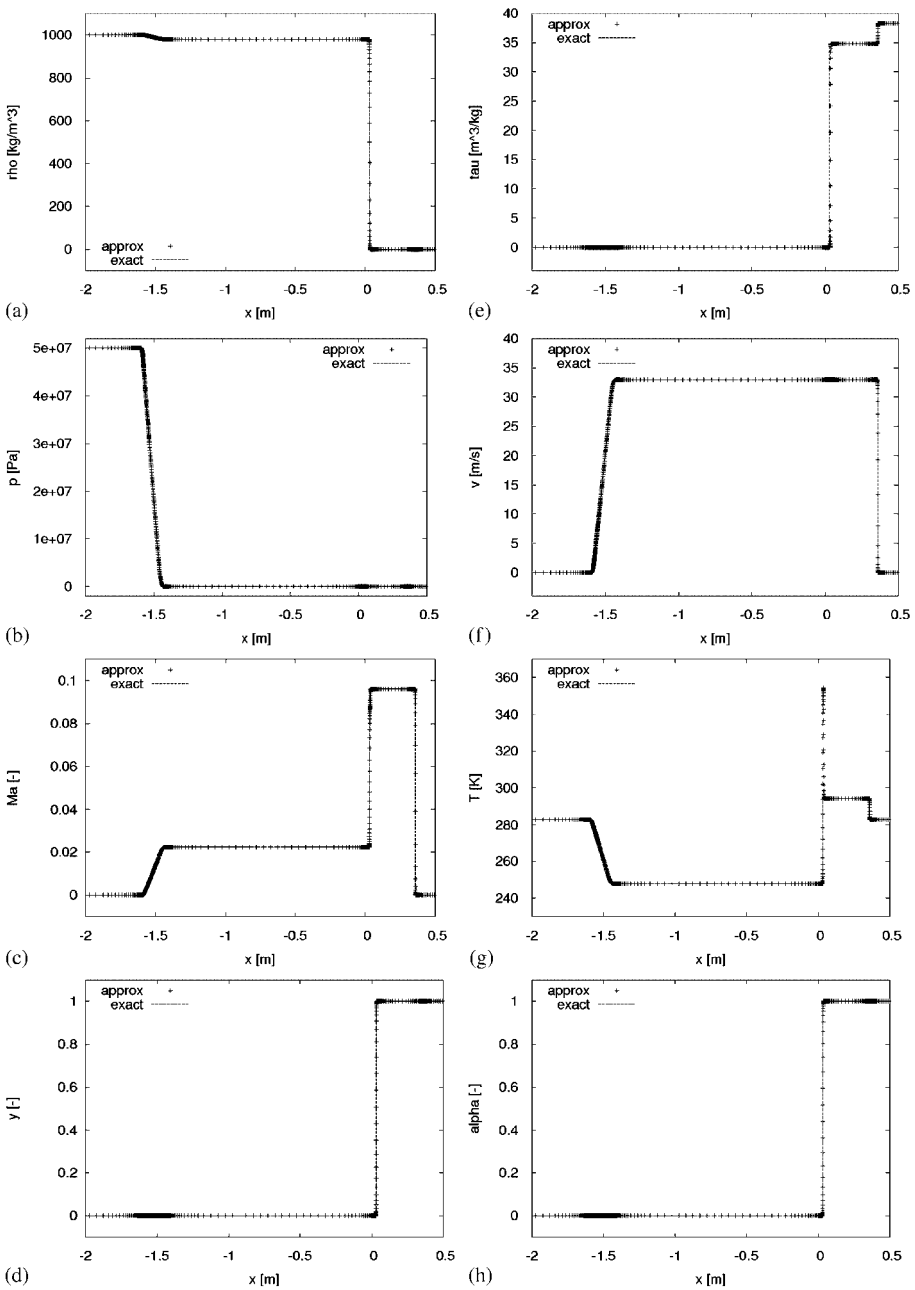

Figure 9. Wave pattern for solution of two-pase Riemann problem at time $t = 1.001984 \times 10^{-3}$ s: (a) density; (b) pressure; (c) Mach number; (d) gas mass fraction; (e) specific volume; (f) velocity; (g) temperature; and (h) gas volume fraction.

DOI: 10.1002/fld

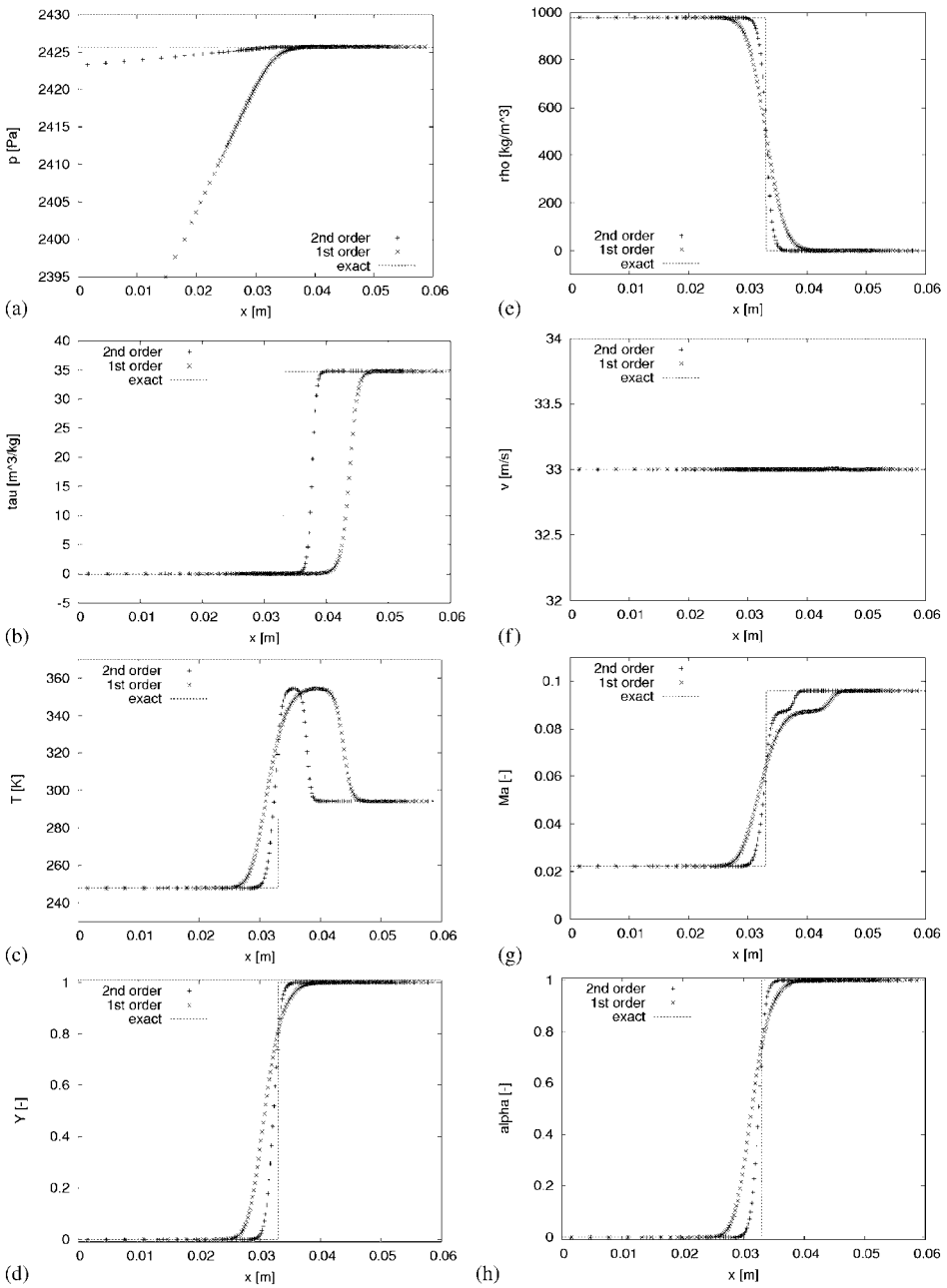

Figure 10. Solution of two-pase Riemann problem at time $t = 1.001984 \times 10^{-3}$ s: contact. (a) pressure; (b) specific volume; (c) temperature; (d) mass fraction; (e) density; (f) velocity; (g) Mach number; and (h) volume fraction.

DOI: 10.1002/fld

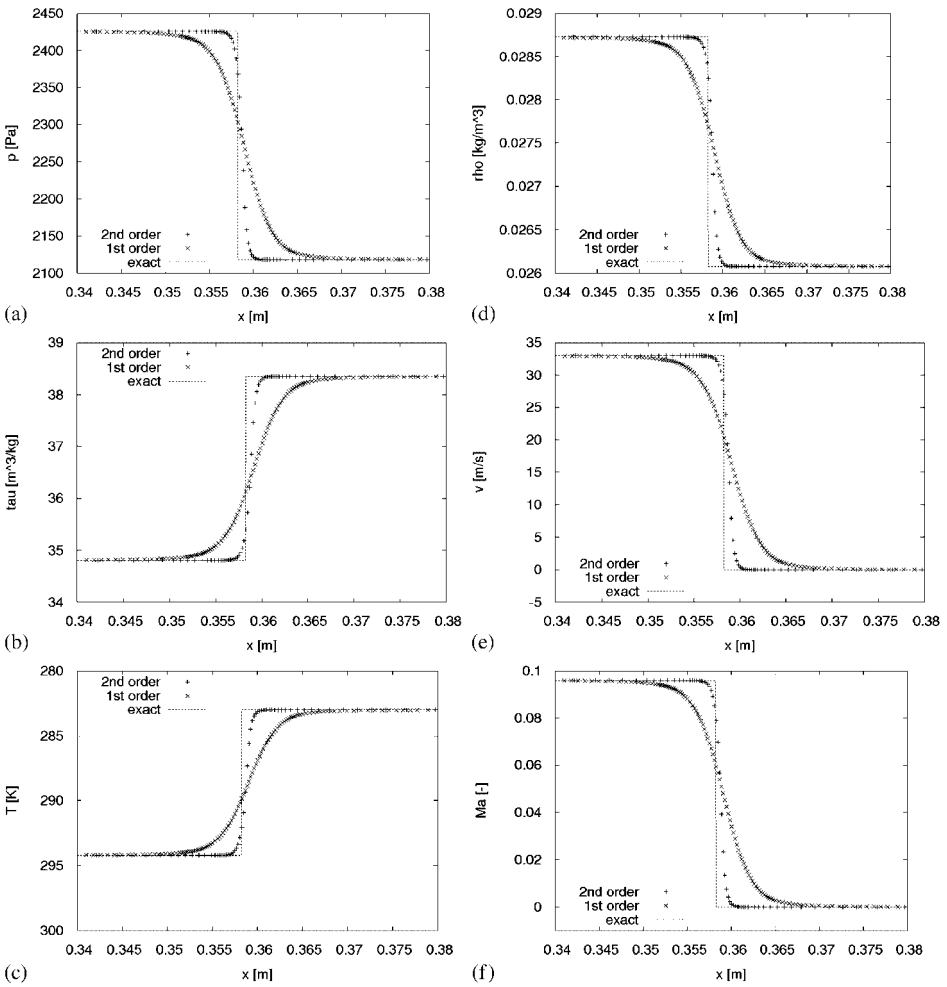

Figure 11. Solution of two-pase Riemann problem at time $t = 1.001984 \times 10^{-3}$ s: shock. (a) pressure; (b) specific volume; (c) temperature; (d) density; (e) velocity; and (f) Mach number.

second-order reconstruction. For first-order reconstruction it is significantly smeared. This is important to note because we want particularly to investigate the behavior of a collapsing gas bubble. For this purpose, it is important to accurately resolve the dynamics inside the bubble. For the rarefaction wave in the liquid, the influence of the higher-order reconstruction is in general not as severe as for the shock wave in the gas phase, see Figure 12. There are slight improvements at the edges of the rarefaction fan. As already discussed above, the second-order reconstruction strongly improves the solution between the rarefaction wave and the material interface, see Figure 12(a). Furthermore, we note that the higher-order reconstruction also improves the solution at the material interface, see Figure 10. Here again this does not hold true for the pressure, see Figure 10(a).

Owing to the strong smearing for the first-order scheme, the efficiency of the adaptive scheme is significantly reduced. To show this we performed several computations for first- and second-order

DOI: 10.1002/fld

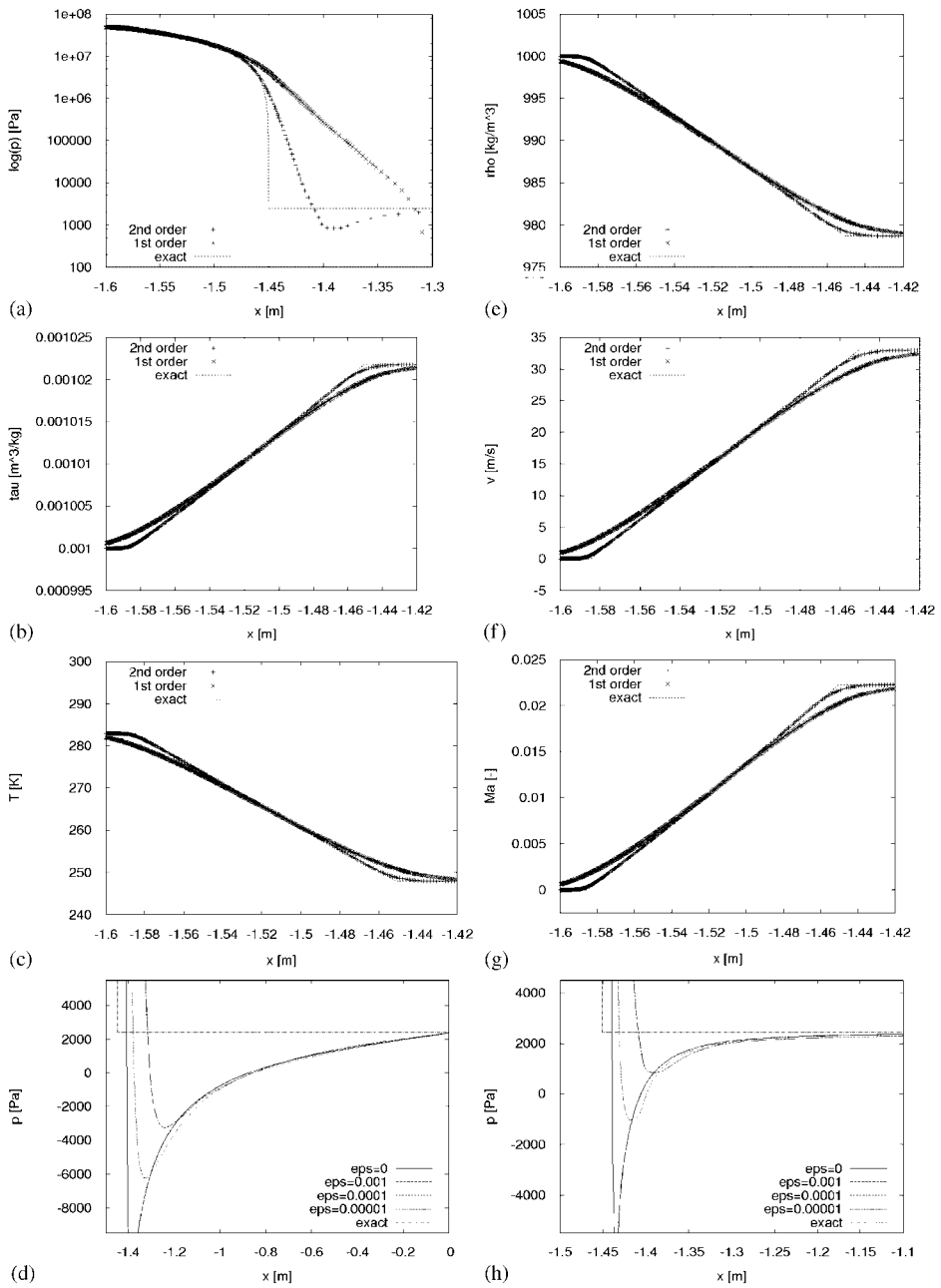

Figure 12. Solution of two-pase Riemann problem at time $t = 1.001984 \times 10^{-3}$ s: rarefaction. (a) pressure; (b) specific volume; (c) temperature; (d) pressure: first order; (e) density; (f) velocity; (g) Mach number; and (h) pressure: second order.

DOI: 10.1002/fld

Table IV. Parameter study w.r.t. threshold value and reconstruction order in case of multilevel time stepping.

	# cells adapt. grid/# cells ref. grid		CPU adapt. scheme/CPU ref. scheme	
ε	First order	Second order	First order	Second order
10^{-2}	0.030	0.024	0.008	0.060
10^{-3}	0.056	0.032	0.002	0.013
10^{-4}	0.098	0.047	0.054	0.020
10^{-5}	0.133	0.072	0.075	0.034
10^{-6}	0.119	0.090	0.081	0.043

Table V. Parameter study w.r.t. threshold value and reconstruction order in case of global time stepping.

	# cells adapt. grid/# cells ref. grid		CPU adapt. scheme/CPU ref. scheme	
ε	First order	Second order	First order	Second order
10^{-2}	0.036	0.026	0.031	0.025
10^{-3}	0.067	0.033	0.057	0.031
10^{-4}	0.111	0.044	0.085	0.057
10^{-5}	0.140	0.055	0.103	0.047
10^{-6}	0.166	0.078	0.114	0.059

in which we vary the threshold value ε. From Tables IV and V we conclude that the number of cells is always higher for the first-order computation. With smaller threshold value ε, the number of grid cells is increasing but less rapidly for the second-order scheme. Therefore, the computational times are always lower for these computations.

These observations hold true for global and multilevel time stepping. However, comparing the results in Tables IV and V we note that the CPU time is always less for multilevel time stepping. As has been observed in previous investigations, cf. [48], less numerical diffusion is introduced because the number of time steps is reduced for the cells on coarser scales. In addition, thresholding is performed less frequently on all scales reducing the threshold error introduced in each grid adaptation step.

From the above discussion we finally conclude that grid adaptation, multilevel time stepping and higher-order reconstruction significantly improve the efficiency and the accuracy of the solution.

4.2. Planar bubble collapse

Now we investigate the collapse of a gas-filled cylindrical bubble of infinite length embedded in an infinite domain of liquid, see Figure 7 (left). Thus, we may consider a 2-D configuration corresponding to a cross-section of the radial collapse of the cylindrical bubble of infinite length. The initial states for the pure phases are the same as for the shock tube problem, see Table II. The radius of the bubble is $R = 0.001\,\mathrm{m}$. The center of the bubble is located in the origin $\mathbf{x} = (0, 0)$ of the coordinate system.

For the numerical simulation we employ rotational symmetry and perform the computation only in the domain $\Omega = [0, 0.01] \times [0, 0.01]$. The coarse grid discretization consists of $N_0 = 25 \times 25$ cells.

DOI: 10.1002/fld

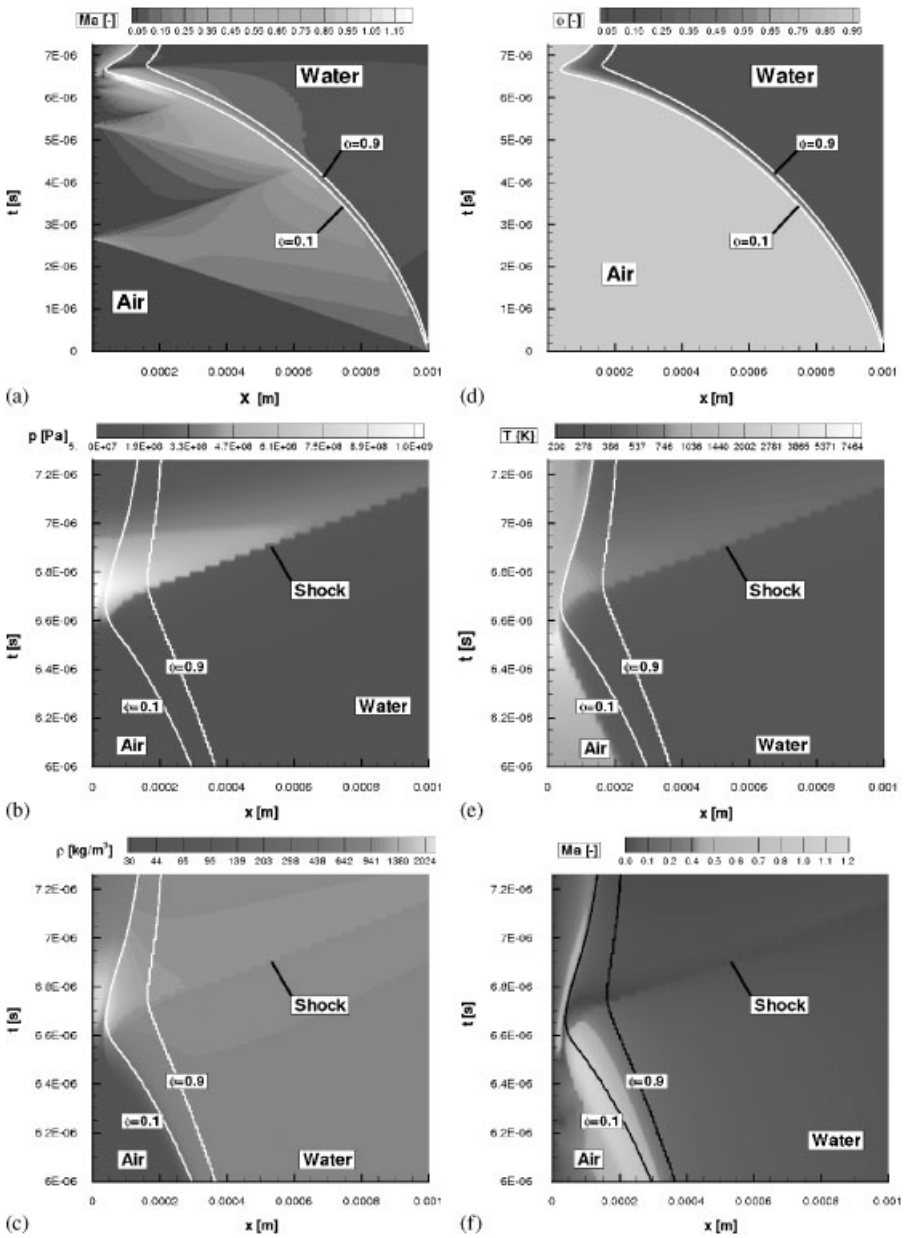

Figure 13. Solution of planar bubble collapse at time $t = 7.26 \times 10^{-6}$ s: (a) Mach number; (b) pressure (zoom); (c) density (zoom); (d) gas mass fraction; (e) temperature (zoom); and (f) Mach number (zoom).

The number of refinement levels is $L = 8$. From this we infer that the (uniform) reference grid on level L is composed of $N_L = 6400 \times 6400$ cells. The time step size is determined after each time step such that the CFL condition holds with CFL number 0.5. Performing $n = 230$ macro time steps with the coarse mesh time-step $\tau_0 = 2^L \tau_L$, this corresponds to a final time of about

DOI: 10.1002/fld

$t = 7.26 \times 10^{-6}$ s. The threshold value is $\varepsilon = 0.001$ and we use the second-order reconstruction of the primitive variables ϱ, $\mathbf{v}$ and p. The computational domain is chosen 10 times larger than the bubble radius to avoid unphysical reflections from the artificial boundary of the computational domain. Since we are not interested in the expansion wave in the water phase, we do not perform grid adaptation outside a domain of radius larger than 0.002 m, which is twice the value of the initial radius of the bubble. This significantly reduces the number of cells in the far field without spoiling the accuracy of the wave processes inside the gas bubble and interactions with the liquid phase. The computations are performed employing multilevel time stepping. The CPU time was about 22.22 h on a PC with an AMD processor Opteron 250.

The wave structure emanating at the phase boundary is the same as for the shock tube problem, see Section 4.1, i.e. a very fast rarefaction wave runs into the water and a slower shock wave runs into the gas, respectively. The phase boundary follows the shock wave first at low speed that leads to a shrinking of the gas bubble. At the same time the shrinking is continuously accelerated and causes compression waves in the bubble. To illustrate the dynamic behavior of the bubble collapse, we extract for each macro time step the data along the x-axis and store them in one file. From this we then visualize the flow along this axis in time, see Figure 13.

The shock wave focuses in the bubble center at time 2.65×10^{-6} s where it is reflected. The average speed of the shock wave is about 377 m/s. This is almost the sound speed corresponding to the initial gas data, i.e. there has been no significant heating of the gas by the first inward running shock, but during the shrinking process temperature increases.

The reflected shock wave runs toward the phase boundary. At time 4.27×10^{-6} s, the shock wave interacts with the phase boundary at radial position $r = 0.0006$ m. From this we deduce an average shock speed of 373 m/s. Owing to the high difference in the acoustic impedance, see Table II state L^* and R, a weak shock is transmitted into the water phase whereas a stronger shock wave is reflected and runs back again toward the bubble center, cf. [71, 72]. The bubble still continues shrinking.

The processes of shock focusing and reflecting in the bubble center and the interaction of the reflected shock wave with the phase boundary is repeating at least four times. Owing to the shrinking process and compression by the shock waves, the gas is significantly heated. Finally at time 6.67×10^{-6} s the bubble reaches its minimal radius of about $R_{\min} = 3.93 \times 10^{-5}$ m. Note that due to the finite resolution of the discretization, not all effects can be resolved in detail. The number of shock focusing processes depends on the initial bubble radius and the exterior pressure in the liquid.

In Figure 13(a) the temporal variation of the Mach number distribution is shown. We note that the phase boundary is accelerated from subsonic speed $\mathrm{Ma} = 0.01$, see Table II, to supersonic speed $\mathrm{Ma} = 1.22$, i.e. $v_{\mathrm{gas}} > 555$ m/s. As can be deduced from the zoom in Figure 13, another shock forms at the bubble in the instant of the largest acceleration and runs into the liquid. According to Hanke, see [19, p. 41], this shock wave is caused by the strong acceleration of the phase boundary that comes to rest when the bubble reaches its smallest radius and becomes accelerated later on in the outward direction.

In Table VI we summarize the extremal data of certain physical quantities at the instant of the bubble collapse. In many publications concerning bubbly liquids, the liquid is assumed to be incompressible. At the instant of the bubble collapse we find that the pressure in the liquid is 1.09×10^9 Pa. At these high values the incompressibility assumption is no longer justified.

Since in our model the two phases are characterized by the volume and mass fraction, the phases are not strictly separated. Owing to the numerical dissipation introduced by the underlying

DOI: 10.1002/fld

Table VI. Quasi-1-D bubble collapse: final states after collapse inside gas bubble.

		Units	Gas (2-D code)	Gas (BUB)
Minimal radius	$R_{\min}$	m	3.93×10^{-5}	7.85×10^{-6}
Maximal pressure	$p_{\max}$	Pa	1.09×10^{9}	1.64×10^{9}
Maximal density	$\varrho_{\max}$	kg/m^3	2.32×10^{3}	4.17×10^{2}
Maximal temperature	$T_{\max}$	K	8.27×10^{3}	1.36×10^{3}
Maximal velocity	$v_{\max}$	m/s	2000	1012
Maximal Mach number of bubble contour	Ma	—	1.22	0.83

finite volume discretization, the phases non-physically mix near the phase boundary causing some numerical phase transition. As can be depicted from Figure 13(d), the numerical phase transition zone is small in the bubble collapse process. However, when the bubble starts growing again, a significant phase transition layer starts forming. This does not occur in the results by Hanke due to the fitting of the phase boundary.

We emphasize that the above observations and conclusions are in agreement with the results reported in [19] for the same configuration. However, there are differences in the mathematical modeling and the numerical discretization. Hanke developed the finite volume code BUB for spherical and cylindrical bubble collapse based on the Navier–Stokes equations using different equations of state for the gas phase, e.g. perfect gas, van der Waals and others, [18, 19]. The material interface separating the liquid and gas phase is fitted. Surface tension is taken into account. In each subdomain the fluid equations are solved with viscosity and heat conduction taken into account in the gas phase, but neglected in the liquid. The material interface is numerically treated according to [73] using front tracking. Thereby mixing of the phases near the phase boundary is suppressed. Note that the BUB code has been validated by the Gilmore equation in case of the *spherical* bubble collapse. Therefore, it is reasonable to expect that this code also provides good results for the cylindrical bubble collapse.

To validate the 2-D computations, we have performed computations with the quasi-1-D code BUB using 200 cells in the gas and 800 cells in the liquid neglecting dissipative effects as well as surface tension. In Figure 14 we compare the Mach number distribution for both computations. The wave pattern is identical. However, the bubble collapse is faster in our 2-D computation due to the higher acceleration of the interface after the first interaction with the shock wave, cf. $Ma_{\max}=1.2$ (2-D) and $Ma_{\max}=0.8$ (BUB). This is due to the higher resolution of the gas phase by BUB, which is fixed because the grid in the two phases is attached to the interface and the grid points are redistributed after each time step. For our 2-D computation, the number of cells is significantly reduced with shrinking bubble radius. Taking this into account, the results can be considered in a qualitatively good agreement.

The lack of viscosity and heat conduction in the present paper may significantly affect the states in the instant of shock focusing in the bubble center. According to the similarity solution derived by Guderley [51] for spherical compression waves where viscosity is neglected, the pressure might increase asymptotically to infinity. Owing to the finite resolution in the discretization, the pressure will be bounded in the computation but it will further increase with higher resolution. Taking into account viscosity, the pressure will stay bounded even with increasing resolution. This has been confirmed numerically in [19].

DOI: 10.1002/fld

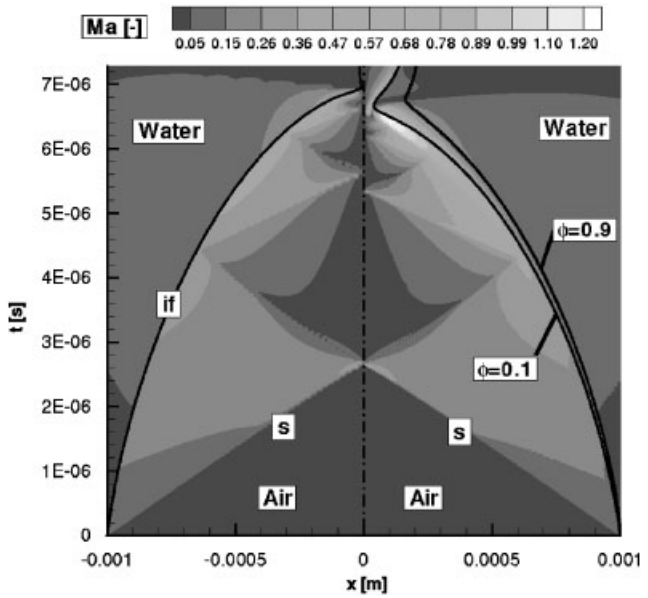

Figure 14. Solution of planar bubble collapse at time $t = 7.26 \times 10^{-6}$ s. Contour plot of the Mach number (left: BUB, right: 2-D code). Dashed line: bubble center, s: shock wave, if: interface.

Since BUB is restricted to quasi-1-D problems, we cannot perform calculations for a bubble next to a wall that is to be investigated next.

4.3. Planar bubble collapse next to a rigid wall

Finally we investigate the bubble collapse for initial conditions as in Section 4.2, see Table II, but next to a rigid plane wall, see Figure 7 (right), i.e. the axis of the cylindrical bubble is parallel to the rigid wall and again it is possible to consider a plane problem. The bubble radius is $R = 0.001$ m and the bubble center is located at $\mathbf{x} = (3R/2, 0)$, i.e. the distance of the bubble center to the planar wall ($x = 0$) is $d = 3R/2$.

The computational domain is determined by $\Omega = [0, 0.1] \times [-0.05, 0.05]$. The coarse grid discretization consists of $N_0 = 25 \times 25$ cells. The number of refinement levels is $L = 8$. From this we infer that the (uniform) reference grid on level L is composed of $N_L = 6400 \times 6400$ cells. The time step size is determined after each time step such that the CFL condition holds with CFL number 0.5. Performing $n = 60$ macro time steps with the coarse mesh time-step τ_0, this corresponds to a final time of about $t = 1.81 \times 10^{-5}$ s. The threshold value is $\varepsilon = 0.001$ and we use the second-order reconstruction of the primitive variables ϱ, $\mathbf{v}$ and p. To avoid unphysical reflections from the boundary of the computational domain, it is set at a distance 100 times the bubble radius away. Since we are not interested in the flow field far away from the wall, we do not perform grid adaptation outside a radius larger than 0.002 m around the initial bubble center. The CPU time was about 11.5 h on a PC with an AMD processor Opteron 250.

The dynamics of the waves that develop in the fluid and their interaction with the wall and the bubble interface can be deduced from the plots of the density gradient magnitude, see

DOI: 10.1002/fld

Figures 15 and 16. Owing to the different scales involved in the liquid and in the gas, these have to be scaled logarithmically to show them simultaneously in one picture, i.e. we present $\log(1+|\nabla\varrho|)$ where the density gradient magnitude is shifted by one to account for vanishing gradients. Owing to the waves and their interactions, the fluid is accelerated. This highly dynamic process is visualized by integral curves of the velocity, i.e. snap shots of the particle path at one time instant where the velocity vector is tangent to the curve, shown in Figures 16(a)–(r) corresponding to the same times as for the density gradient magnitude. The figures for both quantities are superposed with contour lines of the gas fraction to see how the phase interface is affected by the wave interaction process.

First of all, we focus on the waves in the liquid, see Figure 15. In the early stage of the computation the wave structure developing at the phase boundary is the same as for the bubble collapse, see Section 4.2. An expansion wave $R1$ is running into the liquid, see Figure 15(a). Since the bubble is located next to a rigid wall, the expansion wave R1 is reflected as an expansion wave R2 at the wall, see Figure 15(b). Owing to the strong expansion of the liquid behind the wave R2, the pressure drops below zero, i.e. a cavitation region forms. The reflected expansion wave $R2$ again is reflected at the phase boundary, see Figure 15(c). Owing to the low acoustic impedance in the gas and the high acoustic impedance in the liquid, see [71, 72], the reflected wave is a compression wave, i.e. the phase is inverted. This procedure of reflection at the wall and at the phase boundary is continued, see Figure 15(d)–(f), where the phase is maintained at the wall but is inverted at the bubble.

To see the effect of the reflected expansion and compression waves on the gas phase inside the bubble, we zoom into the gas bubble, see Figures 16(a)–(r). In the beginning, there is only a shock wave S running toward the bubble center, see Figure 16(a). When the reflected expansion wave R2 is interacting with the phase boundary, see Figure 16 (b), then it is partially reflected into the liquid as discussed before and partially transmitted into the gas phase, see R3 and T1 in Figure 16(c). We note that the waves are running faster in the liquid than in the gas due to the higher sound speed in the liquid. Owing to the curvature of the bubble contour, the transmitted waves in the gas are defracted, see Figures 16(c)–(e). Therefore the transmitted waves, see for instance T1 in Figures 16(c)–(g), have the shape of a convex lens fixed at the phase boundary, see Figure 16(c). With increasing time, the curvature of the lens becomes stronger, see Figures 16(d) and (e), and, finally, the lens closes to a circle, see Figure 16(f). Then the circular wave focuses inside the bubble at the symmetry line and is reflected, see Figure 16(g). Note that by the transmitted waves the distribution inside the bubble becomes strongly heterogeneous resulting in a pressure gradient of low pressure left to the bubble center and high pressure to the right.

Simultaneously, the shock wave S is focusing in the bubble center, see Figure 16(d), and is reflected there. The reflected shock wave RS1 is running in outward direction toward the bubble interface, see Figures 16(e)–(g). The shock wave is interacting with the transmitted waves. Since in the gas the difference of the acoustic impedance is small, these waves are transmitting without causing reflection waves. Owing to the defraction of the expansion and compression waves, the initially circular shock front flattens at the top and the bottom side and becomes wavy, see Figure 16(g). The reflected shock wave RS1 is interacting with the bubble interface. Owing to the high difference in the acoustic impedance in the two phases, it is being reflected there and running inward again, see RS2 in Figure 16(h). This shock wave focuses and is reflected again as shock wave RS3, see Figure 16(i). This process of shock focusing and shock reflection at the phase boundary is continued. The details of this process cannot be presented here.

DOI: 10.1002/fld

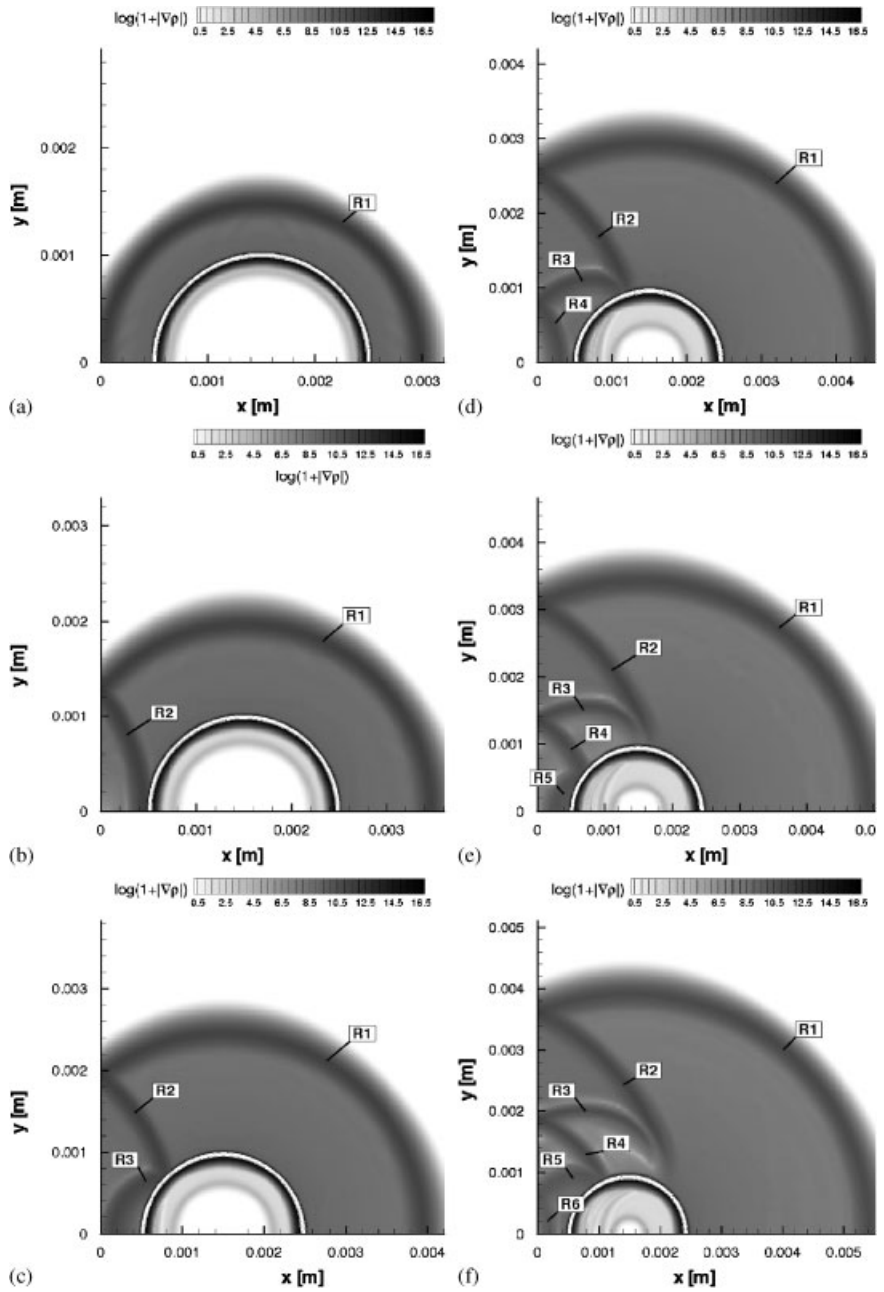

Figure 15. Solution of planar bubble collapse near to a rigid wall: density gradient magnitude and gas fraction: (a) $t = 3.20 \times 10^{-7}$ s; (b) $t = 6.30 \times 10^{-7}$ s; (c) $t = 9.50 \times 10^{-7}$ s; (d) $t = 1.26 \times 10^{-6}$ s; (e) $t = 1.58 \times 10^{-6}$ s; and (f) $t = 1.90 \times 10^{-6}$ s.

DOI: 10.1002/fld

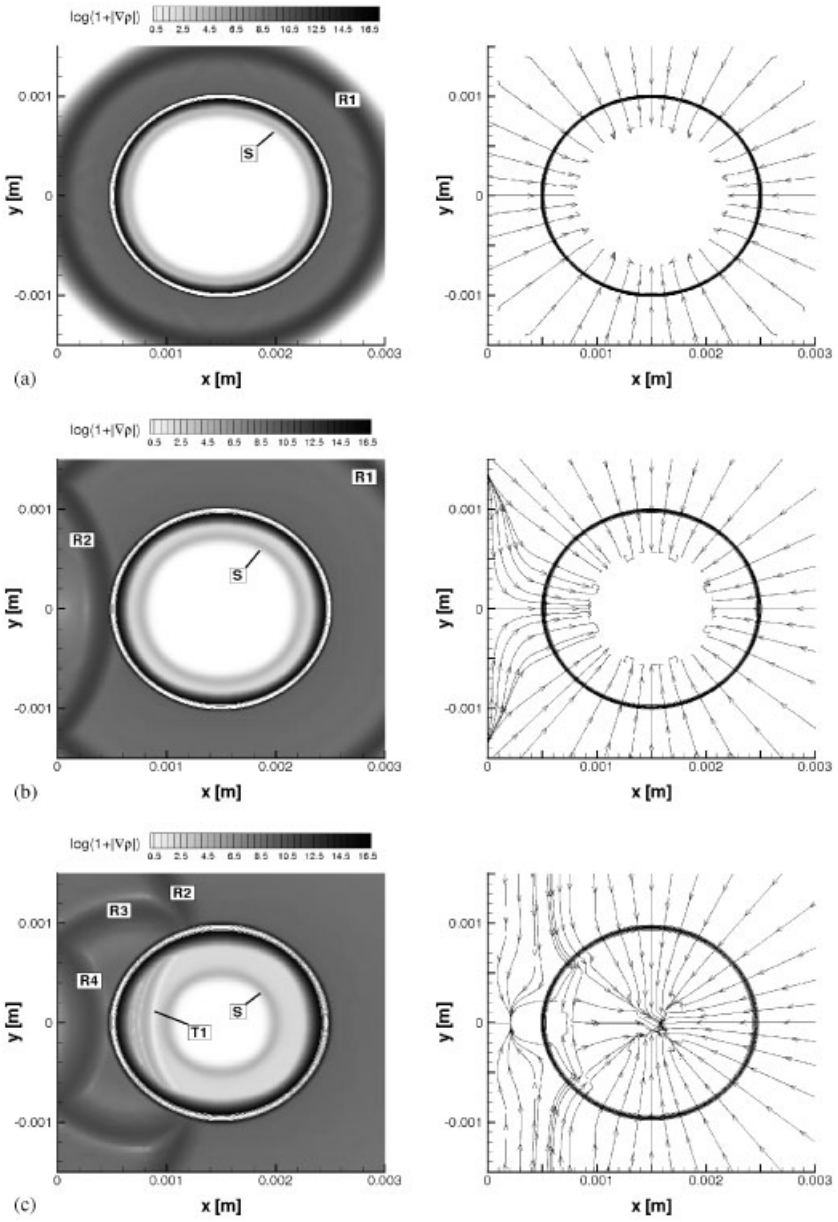

Figure 16. Solution of planar bubble collapse near to a rigid wall: density gradient magnitude (left) and velocity integral curves (right) together with gas fraction. (a) $t=3.20\times10^{-7}$ s; (b) $t=6.30\times10^{-7}$ s; (c) $t=1.26\times10^{-6}$ s; (d) $t=2.53\times10^{-6}$ s; (e) $t=2.84\times10^{-6}$ s; (f) $t=3.16\times10^{-6}$ s; (g) $t=3.79\times10^{-6}$ s; (h) $t=5.14\times10^{-6}$ s; (i) $t=5.65\times10^{-6}$ s; (j) $t=6.32\times10^{-6}$ s; (k) $t=7.11\times10^{-6}$ s; (l) $t=7.89\times10^{-6}$ s; (m) $t=8.50\times10^{-6}$ s; (n) $t=9.30\times10^{-6}$ s; (o) $t=9.82\times10^{-6}$ s; (p) $t=1.21\times10^{-5}$ s; (q) $t=1.35\times10^{-5}$ s; and (r) $t=1.73\times10^{-5}$ s.

DOI: 10.1002/fld

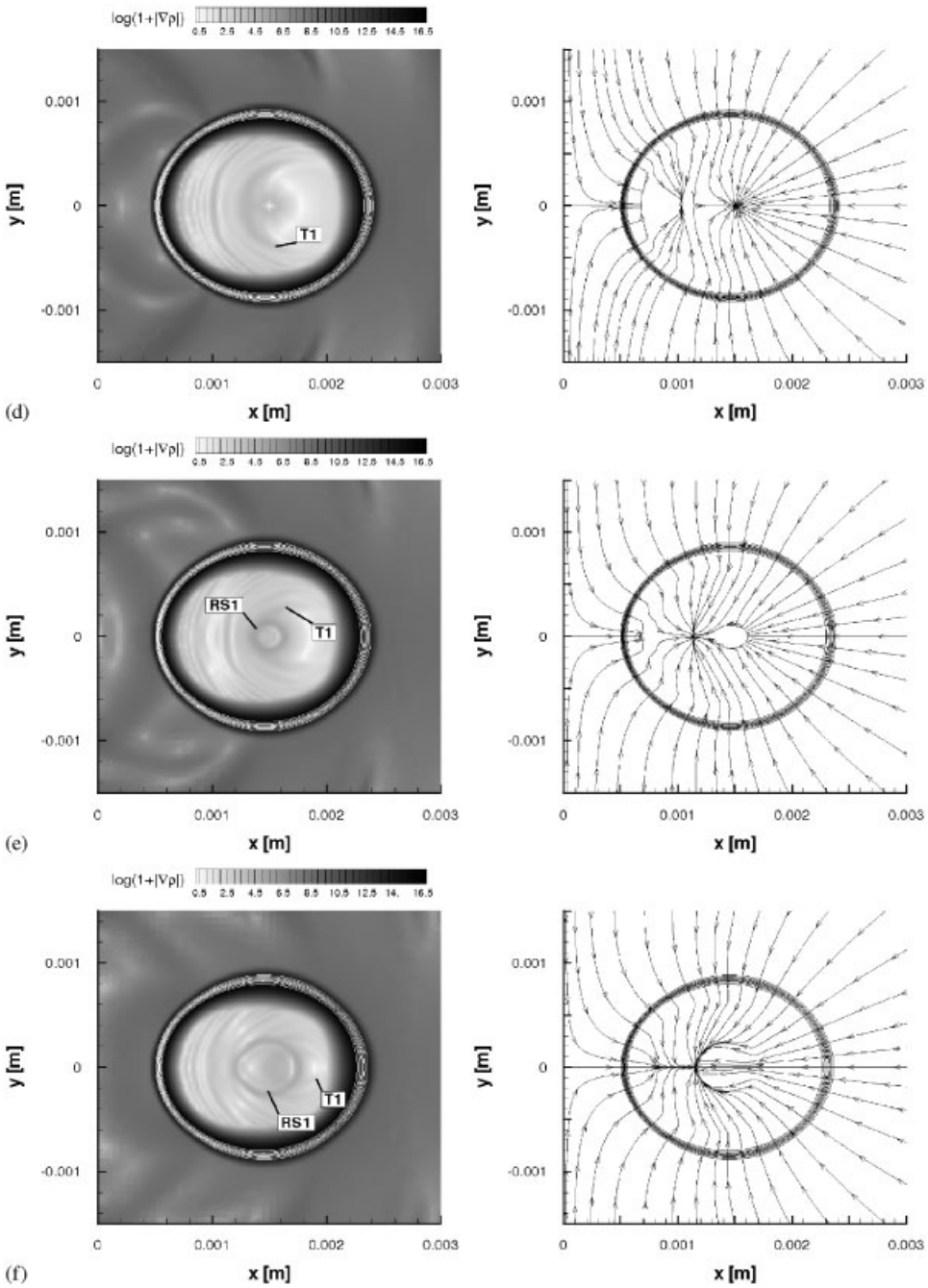

Figure 16. *Continued.*

DOI: 10.1002/fld

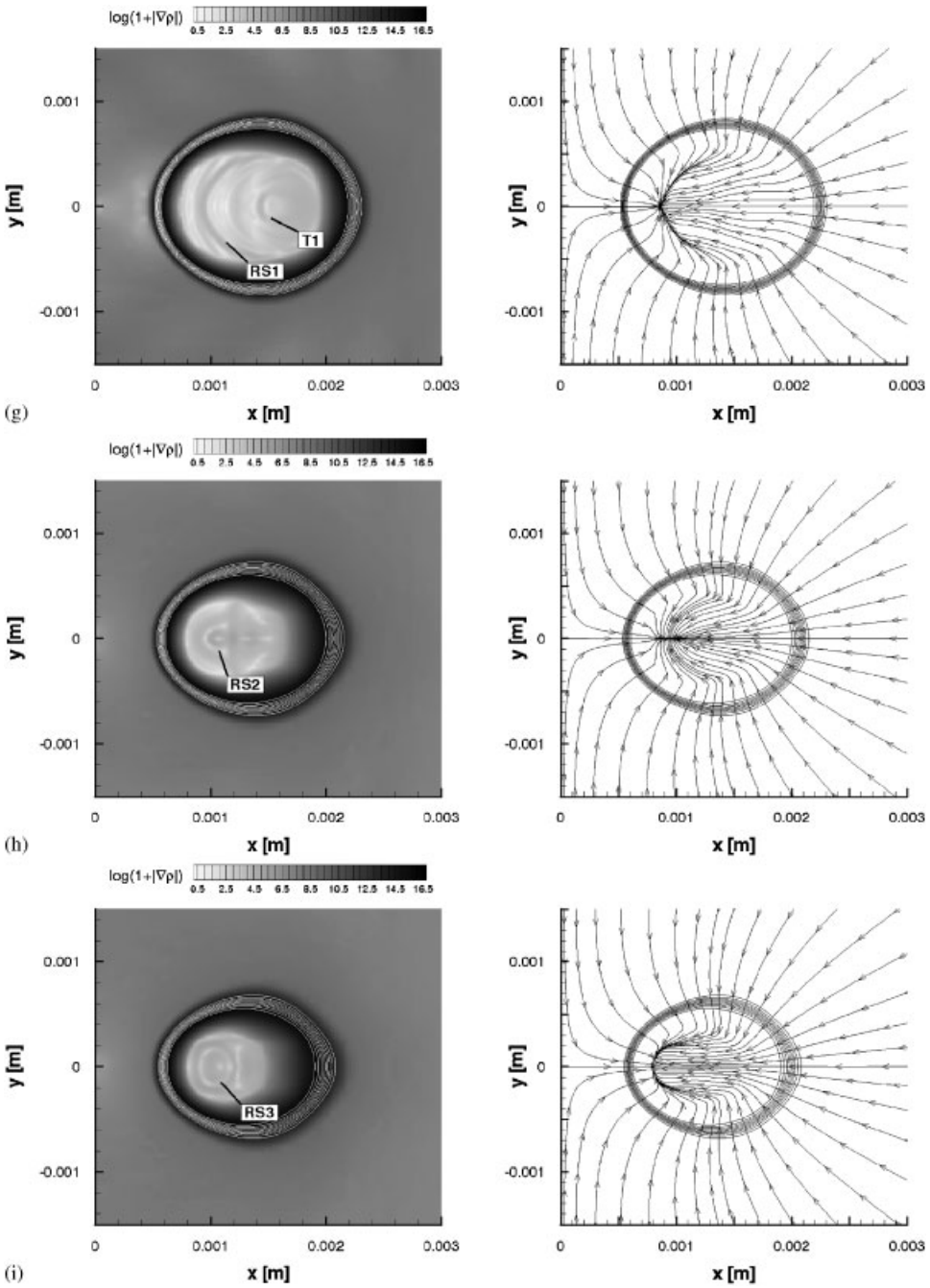

Figure 16. *Continued.*

DOI: 10.1002/fld

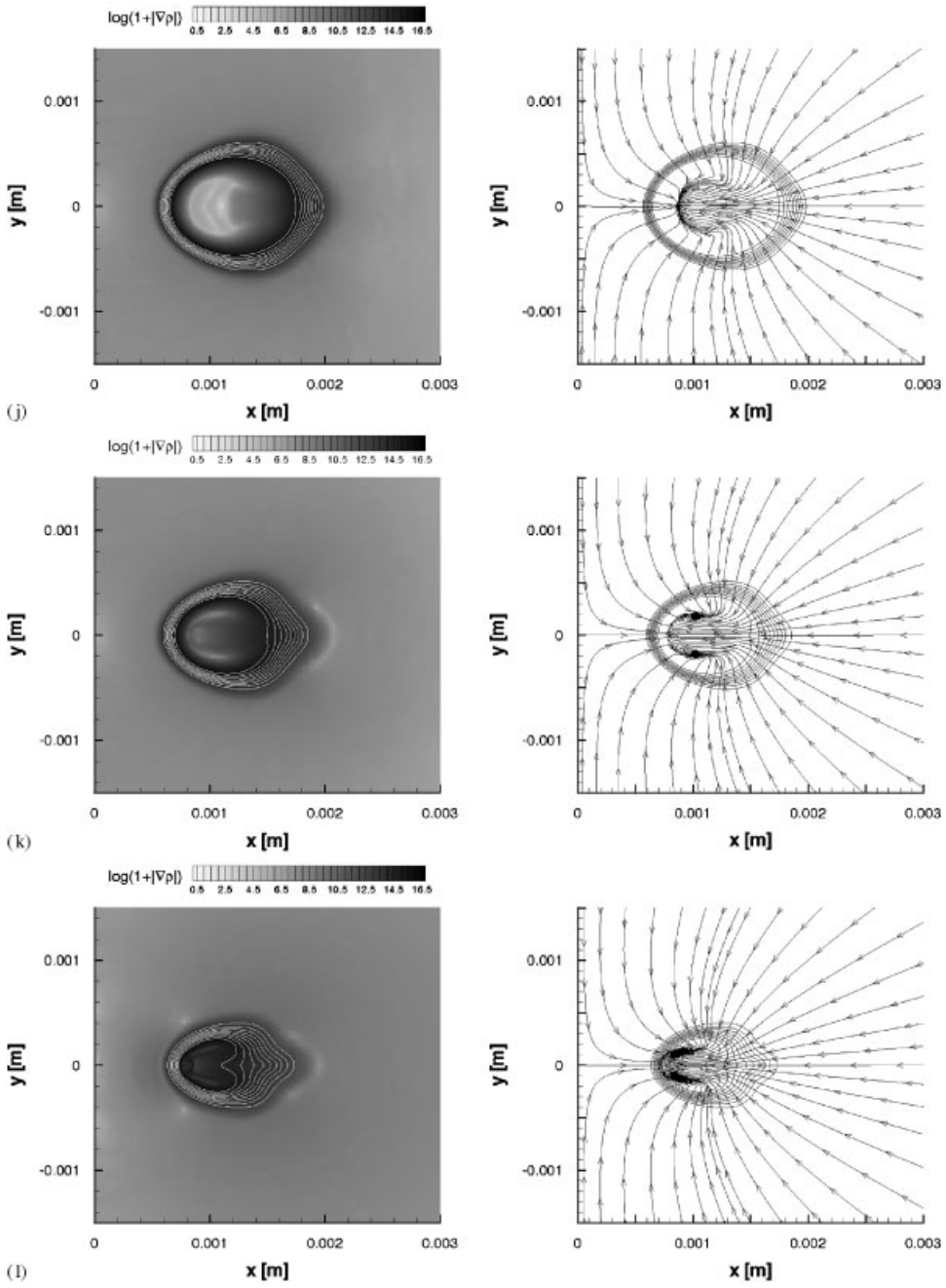

Figure 16. *Continued.*

DOI: 10.1002/fld

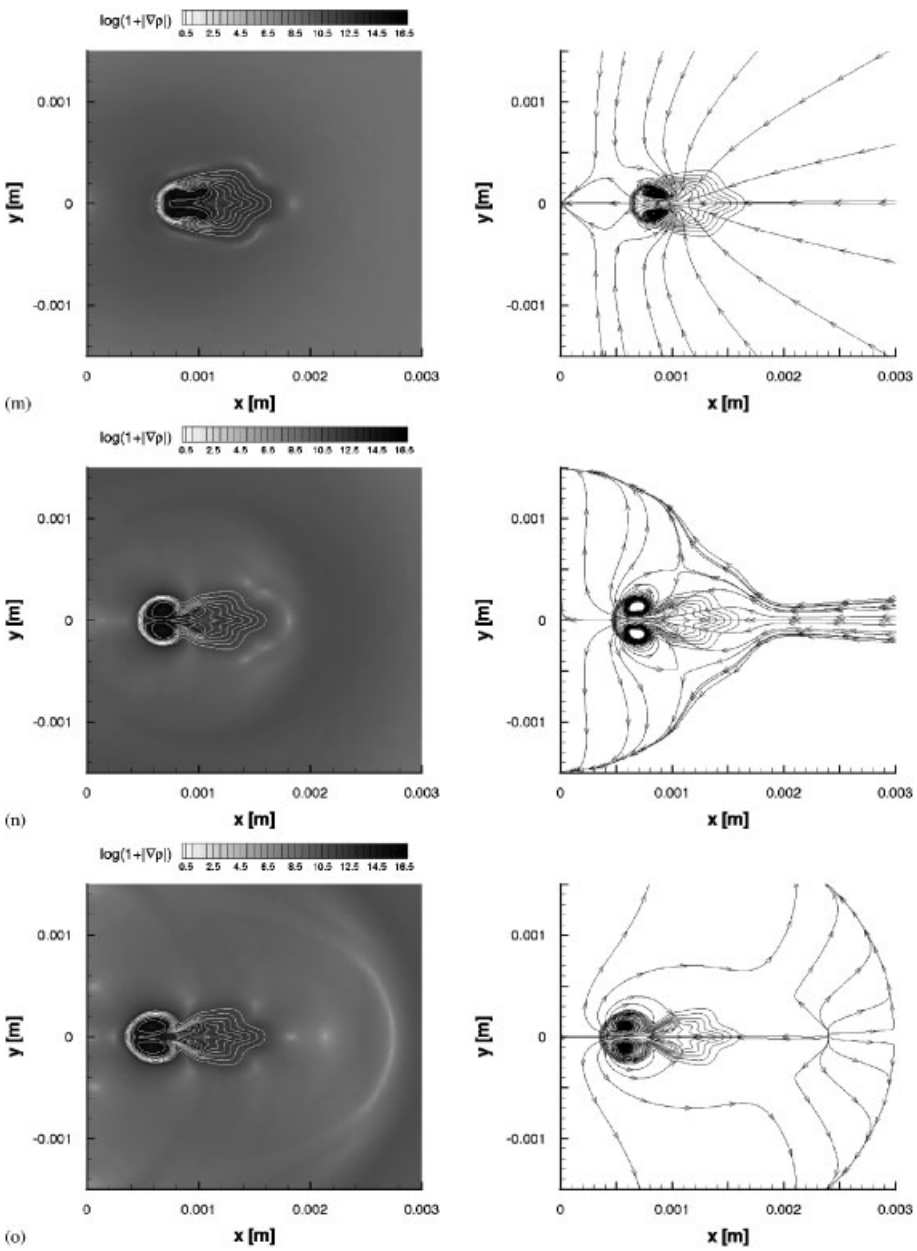

Figure 16. *Continued.*

DOI: 10.1002/fld

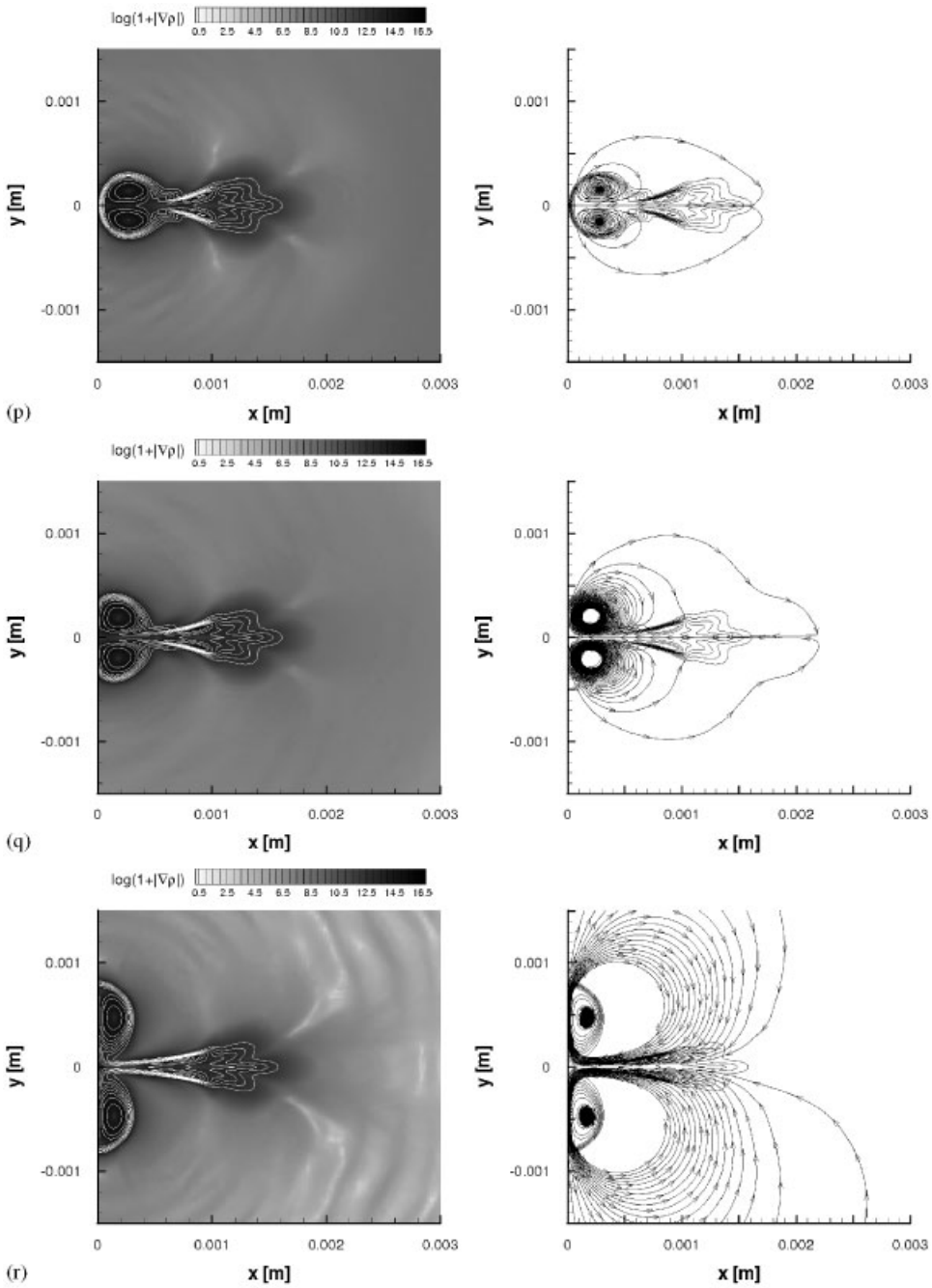

Figure 16. *Continued.*

DOI: 10.1002/fld

Owing to the wave processes in the liquid and in the gas, the flow field is accelerated. The dynamics of the acceleration can be depicted from the integral curves of the velocity presented in Figure 16(a)–(r). Starting from a flow at rest, the flow field is accelerated toward the bubble center when the expansion wave R1 and the shock wave S pass, see Figure 16(a). The velocity field is rotational symmetric as long as the expansion wave R1 has not been reflected at the wall. The reflection of wave R1 leads to a distortion of the symmetry. Behind the reflected expansion wave R2, a low pressure regime develops that extends with increasing time into the far field. Therefore, the liquid is accelerated in the direction of the symmetry line and near the wall it is moving almost parallel to the wall. At the symmetry line the liquid is then deflected and directed toward the gas bubble, see Figure 16(b)–(m). While the flow is deflected near the wall, the flow away from the wall is directed toward the bubble center, see Figure 16(b) and (c). Inside the bubble the gas is no longer moving toward the bubble center when the transmitted waves, see for instance T1, pass but is deflected toward the symmetry line. When the shock wave S focuses in the bubble center, see Figure 16(d), it is reflected there and the flow behind the reflected shock wave RS1 is now accelerated in the outward direction, see Figure 16(e)–(g). However, this acceleration is not sufficient to revert the flow direction due to the underlying velocity field caused by the inward running shock S and due to the pressure gradient caused by the transmitted expansion waves as discussed above. Therefore, the gas in the right part of the bubble is still moving inward. On the other hand, behind the transmitted waves, see for instance T1, the gas is accelerated toward the bubble center, see Figure 16(d). Owing to the strong acceleration of the gas behind the reflected shock wave RS1, the gas behind the transmitted waves is repelled, see Figure 16(e)–(g). A front is forming where the gas from both sides is deflected toward the symmetry line where the integral curves of the velocity coincide in a stagnation point. Since the gas is more rapidly accelerated at the right side of the deflection front than at the left side, the stagnation point is moving toward the wall, see Figure 16(h)–(k). Owing to the ongoing process of shock wave focusing in the bubble and shock reflection at the phase boundary, the underlying flow field is further accelerated without changing the overall flow direction in the regions left and right from the deflection front. However, the flow attached to this front changes its direction. In the beginning, the attached flow is directed toward the stagnation point, see Figure 16(f)–(j), whereas it is moving away from the stagnation point in the outward direction at some later time, see Figure 16(k). This phenomenon could be associated with the so-called *counter jet* sometimes observed in experiments. Since the gas is more rapidly accelerated to the right of the deflection front than to the left, a velocity gradient develops across the front. Owing to this velocity gradient, two vortices are forming inside the gas bubble above and below the symmetry line, rotating clockwise and counter-clockwise, respectively, see Figure 16(j)–(m). The rotation of the vortices causes the gas to concentrate in the center of the vortices. This results in a high compression of the gas. In the core of the vortices, we compute a pressure of about 300 bar, a density of about $250\,\mathrm{kg/m^3}$ and a temperature of about 600 K. When the gas mass is concentrating in the core of the vortices, the gas bubble splits into two parts and a liquid jet is forming, see Figure 16(m) and (n). This jet is directed toward the wall due to the clockwise and counter-clockwise rotation of the vortices above and below the symmetry line, respectively, see Figure 16(m). The two gas bubbles cause a bottleneck for the liquid due to the high density of the gas. Therefore, the liquid is accelerated toward the wall through this orifice, see Figure 17. The maximal speed of about 900 m/s is reached at time $t = 9.07 \times 10^{-6}$ s, see Figure 17(b), at the symmetry line between the two vortices. This value corresponds to a Mach number of 1.6. At this instant, the gas is at rest in the center of the vortices whereas the velocity is about 300 m/s directed away from the wall at the furthest point of the bubble contours from the symmetry line.

DOI: 10.1002/fld

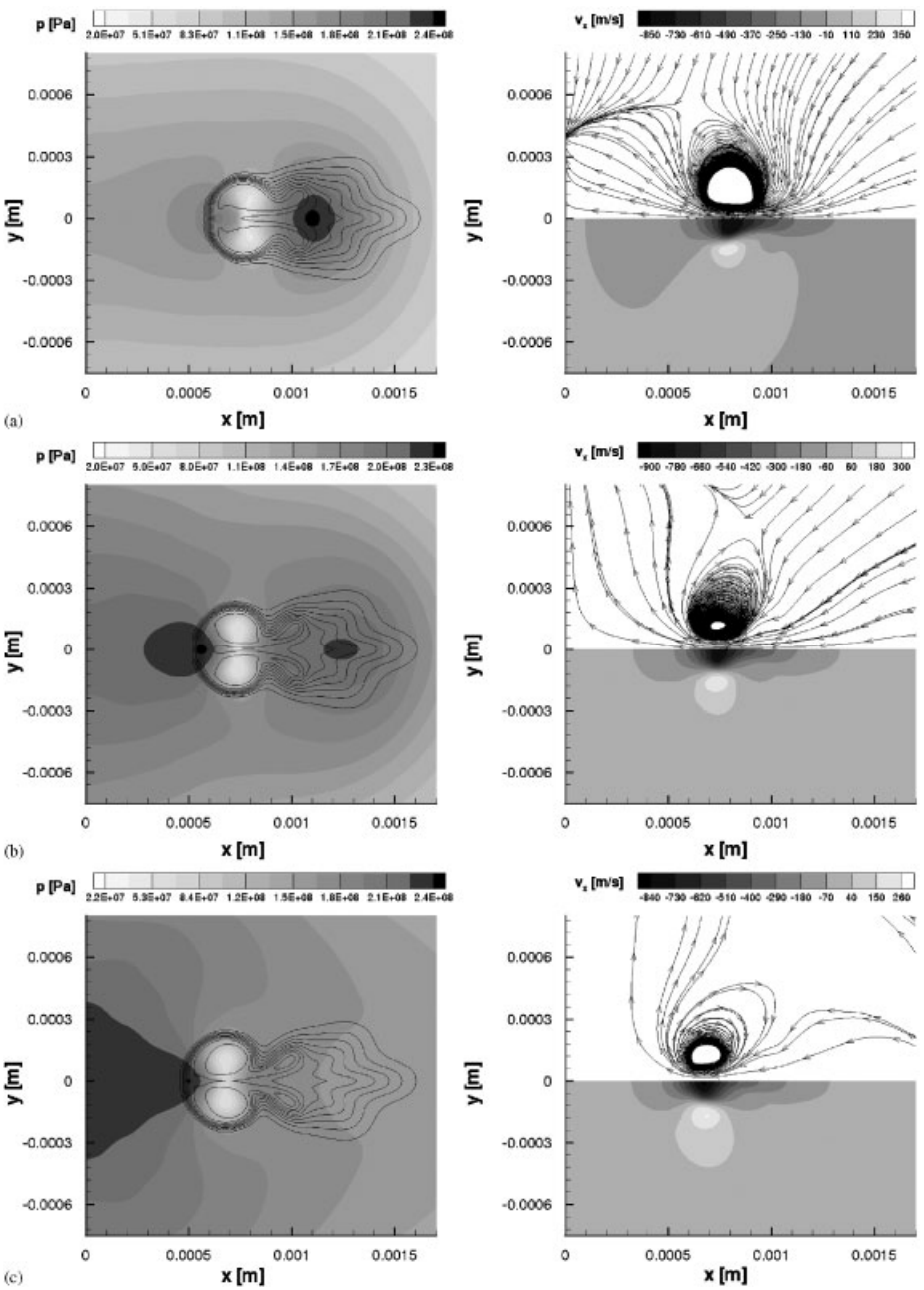

Figure 17. Solution of planar bubble collapse near to a rigid wall: Pressure and gas fraction (left) and x-velocity and velocity integral curves (right): (a) $t = 8.80 \times 10^{-6}$ s; (b) $t = 9.07 \times 10^{-6}$ s; and (c) $t = 9.33 \times 10^{-6}$ s.

DOI: 10.1002/fld

When the liquid is accelerated through the orifice, the pressure is increasing before the bottleneck resulting in a high pressure region of about 2400 bar, see Figure 17(a). Since the liquid is expanding behind the orifice, the high pressure region is squeezed through this bottleneck and shot like a projectile toward the wall where it hits at high pressure, about 5 times that of the undisturbed liquid, see Figure 17(a)–(c). The impact of the high pressure might be the cause of material damage as has been observed in experiments, cf. [3, 6, 7].

When the liquid jet hits the wall, another stage in the bubble collapse begins. The water supplied by the jet is deflected to both sides of the symmetry axis due to the resistance of the wall. Since this liquid is moving at higher speed than the liquid supplied from the undisturbed flow, it represses the latter, see Figure 16(n). Because of this process the two vortices and, attached to them, the gas bubbles start to move toward the wall where they are deflected in the upward and downward direction, see Figure 16(o)–(r). If the high temperature gas bubbles came into contact to the wall, it may cause some material damage. However, in our computations the gas bubbles are surrounded by a phase transition zone where the temperature is decreasing significantly.

We conclude the numerical investigation by some comments on the phase interface. Owing to the stiffened gas model, the phase boundary is not necessarily a sharp discontinuity but may become diffusive. In the beginning, the interface is slightly accelerated by the shock wave S resulting in a slow shrinking process of the gas bubble, see Figure 16(a)–(g). When the shock wave RS2 is reflected at the phase interface, the phase boundary is significantly accelerated, see Figure 16(h) and (i). Owing to the inertia of the liquid, a phase transition zone develops filled with a mixture of gas and liquid, see Figure 16(j)–(r). By the vortices forming inside the gas bubble, the pure gas is transported to the core of these vortices. In Figure 16(k) and (l) we see that the gas fraction contour corresponding to pure gas starts bulging and is finally penetrated by the gas–liquid mixture, see Figure 16(m). In the end, only two bubbles filled with pure gas remain, see Figure 16(n)–(r).

Finally, we discuss the simulation setup and the numerical results in the context of experimental bubble research with laser-produced cavitation bubbles, cf. [12–14], because the results display several phenomena discussed in these papers. However, note that a direct comparison with the experimental results is not possible, because (i) initial data of the gas state just after forming of the cavitation bubble by the laser pulse can be hardly measured and (ii) the computations are performed for a cylindrical bubble instead of a spherical bubble usually investigated in the experiments.

The experimental results are typically classified by means of the dimensionless parameter $\overline{\gamma}=d/R$ where d is the distance of the bubble center to the wall and R the maximum bubble radius, cf. [12]. In [13] it has been found experimentally for $\overline{\gamma}\gtrsim 1.5$ that the liquid jet does not reach the solid wall and shock waves are assumed to contribute the bulk of the damage to the wall. For $\overline{\gamma}\lesssim 1.5$, the jet does reach the wall and, in addition, contributes to the damage.

For the configuration at hand it turns out that $\overline{\gamma}=1.5$. Therefore, the simulation lies in the uncertain grey area between these regions of the parameter. The results suggest that the liquid jet does indeed reach the wall, but the reason for this happening is not entirely clear. The assumptions, in particular neglecting gravity, may affect whether the jet reaches the wall or not.

Another phenomenon associated with $1\lesssim\overline{\gamma}\lesssim 3$ is the counter jet, cf. [12, 14]. The numerical results show some outward directed flow, see Figure 16(k) onward that might be related to this physical feature.

DOI: 10.1002/fld

5. CONCLUSION

The stiffened gas model of Saurel and Abgrall [11] has been successfully extended to a higher-order scheme on locally refined grids. Multiscale-based grid adaptation techniques [42, 43] have been employed to improve the efficiency of the scheme. This allows for a locally high resolution that is needed to resolve accurately the local physical effects in the bubble collapse process. Since this process is highly dynamical, the time discretization is explicit. Therefore, the CFL condition is very restrictive because of the small cells used in the high refinement levels. For the cells on the coarser discretization levels, we use a multilevel time stepping strategy that allows for larger time steps on coarser scales. This has been recently developed in combination with the multiscale-grid adaptation, cf. [48–50]. This strategy had to be modified taking into account the non-conservative upwind discretization of the evolution equations for the material parameters.

The accuracy and the efficiency of the resulting adaptive scheme has been validated by means of a two-phase Riemann problem. It turned out that the accuracy is significantly improved by the second-order reconstruction in comparison with the original scheme of Saurel and Abgrall that is of first order only. In addition, the CPU time as well as the memory resources are tremendously reduced because of the grid adaptation and the multilevel time stepping strategy. However, the non-conservative discretization of the evolution equations for the material parameters results in some slight deviation of the shock position from the exact position. Moreover, an additional temperature jump can be observed in the numerically smeared contact discontinuity. For inviscid computations, this has no effect on the computation, but for computations including viscosity it might become significant if the viscosity coefficient is temperature dependent.

The scheme has then been applied to investigate the collapse of a free planar gas bubble at low pressure and density surrounded by water at high density and pressure. A shock wave runs inside the gas bubble between bubble center and phase boundary where it is focused and reflected several times. By this process the gas undergoes a strong compression resulting in a significant heating. The phase boundary is accelerated toward the bubble center where it collapses and reaches a minimal radius that is about 25 times smaller than the original bubble radius. In the instant of the collapse a shock wave runs into the water that results in a significant compression of the liquid. At these high values the incompressibility assumption is no longer justified. Owing to the compression inside the bubble, density, pressure and temperature increase by several orders of magnitude. For more realistic values, the gas should be modeled by a real gas equation of state rather than the perfect gas law. We emphasize that these observations and conclusions are in agreement with the results reported in [18, 19] for the same configuration but performing quasi-1-D computations exploiting spherical symmetry.

Finally we investigated the bubble collapse next to a rigid wall. The dynamics of the resulting flow field can be separated into three stages. In a first stage, a low pressure regime is developing between the wall and the gas bubble. This is caused by expansion and compression waves running between the wall and the bubble where they are reflected. Owing to the low acoustic impedance in the gas and the high acoustic impedance in the liquid, the phase is inverted when the wave is reflected at the bubble contour, but it remains unchanged when it is reflected at the wall. At the same time, a shock wave runs inside the bubble toward the bubble center. Owing to transmitted expansion and compression waves at the interface, the pressure distribution also becomes asymmetric inside the bubble. When the shock wave focuses in the bubble center, a second stage starts where a liquid jet forms that penetrates the bubble at the symmetry line and is directed toward the wall. This process is caused by the formation of two vortices inside the gas bubble, which cause the

DOI: 10.1002/fld

gas to concentrate in two almost rotational symmetric gas bubbles above and below the symmetry axis. The small distance between the two vortices causes a bottleneck for the liquid that acts as a nozzle in which the liquid is significantly accelerated. In front of this bottleneck, a high pressure zone forms in the liquid where the pressure is about 5 times higher than in the undisturbed liquid. This high pressure liquid is then squeezed through the bottleneck and directed toward the wall where it hits with high pressure. The impact of the high pressure might be the cause of material damage, but an analysis of this would require solution of a coupled fluid–structure problem with appropriate modeling of elastic–plastic stress waves in the solid wall, see [25, 74]. In experiments [13] it has been found that the jet impact contributes to the damage. In case the jet does not reach the wall, shock waves contribute the bulk of the damage to the wall. However, for the investigated configuration choosing $\overline{\gamma}=1.5$, it is not clear whether the jet should reach the wall or not. When the jet hits the wall, the third stage of the flow process starts. The liquid supplied by the jet is deflected at the wall on both sides of the symmetry axis and pushes away the water supplied from the free stream from above and below. In the wake of the jet, the system of the split bubbles and the vortices start moving toward the wall where they are deflected up and down the symmetry axis.

The numerical investigation clearly indicates that the bubble splitting and the formation of the liquid jet is essentially caused by the acceleration of the gas inside the bubble due to the shock wave focusing in the center and its reflection at the phase interface as well as its interaction with the transmitted compression and expansion waves. Therefore, the frequently made assumption of a homogeneous state inside the gas bubble can no longer be considered to be admissible.

So far viscosity and heat conduction as well as surface tension have not been taken into account. These might affect the processes of bubble collapse, jet formation and bubble splitting. Furthermore, the phase boundary is diffusive due to the modeling of the two-phase fluid by a single compressible medium. It would be interesting to compare the results with sharp interface model using level set methods, cf. [75]. This, in particular, would allow us to use different models for the gas and the liquid, respectively. For this purpose, we currently are performing numerical investigations of the laser-induced cavitation bubbles by means of 1-D rotational symmetric flows where we compare the stiffened gas approach with the real ghost fluid method [10].

The ultimate goal of our future work will be the investigation of the fully 3-D bubble collapse. As can be observed in experiments with laser-induced cavitation bubbles [12–14], the flow field can be assumed to be rotationally symmetric in the first bubble collapse. However, in the rebound the bubble shape becomes asymmetric due to instabilities. Therefore, rotationally symmetric computations can only be an intermediate step. Finally, there must be fully 3-D computations that require a parallelized implementation of the numerical methods.

ACKNOWLEDGEMENTS

The authors would like to thank Dr Sigrid Andreae (Hilti Vaduz, Liechtenstein) and Dr Gerd Britten (BMW Munich, Germany) for their assistance in visualizing the numerical results and providing the computations by the BUB code. This work has been performed with funding by the Deutsche Forschungsgemeinschaft in the DFG–CNRS-Research group FOR 563 '*Micro-Macro Modelling and Simulation of Liquid-Vapor Flows*'.

DOI: 10.1002/fld

REFERENCES

1. Naudé CF, Ellis AT. On the mechanism of cavitation damage by nonhemispherical cavities collapsing in contact with a boundary. *Transactions of the ASME D, Journal of Basic Engineering* 1961; **83**:648–656.
2. Benjamin TB, Ellis AT. The collapse of cavitation bubbles and the pressure thereby produced against solid walls. *Philosophical Transactions of the Royal Society of London A* 1966; **260**:221–240.
3. Philipp A, Lauterborn W. Cavitation erosion by single laser-produced bubbles. *Journal of Fluid Mechanics* 1998; **361**:75–116.
4. Ohl CD, Ikink R. Shock-wave-induced jetting of micron-size bubbles. *Physical Review Letters* 2003; **90**:214502-1–4.
5. Ohl CD, Wolfrum B. Detachment and sonoporation of adherent HeLa-cells by shock wave-induced cavitation. *Biochimia Biophysica Acta* 2003; **1624**:131–138.
6. Brujan EA, Nahen K, Schmidt P, Vogel A. Dynamics of laser-induced cavitation bubbles near an elastic boundary. *Journal of Fluid Mechanics* 2001; **433**:251–281.
7. Brujan EA, Nahen K, Schmidt P, Vogel A. Dynamics of laser-induced cavitation bubbles near elastic boundaries: influence of the elastic modulus. *Journal of Fluid Mechanics* 2001; **433**:283–314.
8. Akhatov I, Lindau O, Topolnikov A, Mettin R, Vakhitova V, Lauterborn W. Collapse and rebound of a laser-induced cavitation bubble. *Physics of Fluids* 2001; **13**(10):2805–2819.
9. Abgrall R, Karni S. Computations of compressible multifluids. *Journal of Computational Physics* 2001; **169**(2):594–623.
10. Wang CW, Liu TG, Khoo BC. A real ghost fluid method for the simulation of multimedium compressible flow. *SIAM Journal on Scientific Computing* 2006; **28**(1):278–302.
11. Saurel R, Abgrall R. A simple method for compressible multifluid flows. *SIAM Journal on Scientific Computing* 1999; **21**(3):1115–1145.
12. Lindau O, Lauterborn W. Cinematographic observation of the collapse and rebound of a laser produced cavitation bubble near a wall. *Journal of Fluid Mechanics* 2003; **479**:327–348.
13. Shima A, Takayama K, Tomita Y. Mechanism of impact pressure generation from spark-generated bubble Collapse near a wall. *AIAA Journal* 1983; **21**(1):55–59.
14. Vogel A, Lauterborn W, Timm R. Optical and acoustic investigations of the dynamics of laser-produced cavitation bubbles near a solid boundary. *Journal of Fluid Mechanics* 1989; **206**:209–338.
15. Westenberger H. On the dynamics of momentum transport in bubbly compressible liquids. *Ph.D. Thesis*, RWTH Aachen, 1987 (in German).
16. Best JP, Kucera A. A numerical investigation of non-spherical rebounding bubbles. *Journal of Fluid Mechanics* 1992; **245**:137–154.
17. Lee M, Klaseboer E, Khoo C. On the boundary integral method for the rebounding bubble. *Journal of Fluid Mechanics* 2007; **570**:407–429.
18. Hanke M, Ballmann J. Multiresolution algorithms for the numerical solution of hyperbolic conservation laws. *ZAMM* 1998; **78**(Suppl. 1):453–454.
19. Hanke M. Analysis and evaluation of physical models for large variation of state in collapsing bubbles. *Master Thesis*, RWTH Aachen, 1998 (in German).
20. Monaghan J. Simulating free surface flows with SPH. *Journal of Computational Physics* 1994; **110**:399–406.
21. DiLisio R, Grenier E, Pulvirenti M. On the convergence of the SPH method. *Computers and Mathematics with Applications* 1998; **35**:95–108. Special issue devoted to Simulation Method in Kinetic Theory.
22. Hyman J. Moving mesh methods for partial differential equations. *Mathematics Applied to Science* 1986; 129–153.
23. Chern IL, Glimm J, McBryan O, Plohr B, Yaniv S. Front tracking for gas dynamics. *Journal of Computational Physics* 1986; **62**:83–110.
24. Klingenberg Ch, Plohr B. An introduction to front tracking. *Multidimensional Hyperbolic Problems and Computations*, *Proceedings of the IMA Workshop*, Minneapolis/MN (U.S.A) 1989; *IMA Volumes in Mathematics and its Applications* 1991; **29**:203–216.
25. Dickopp Ch. A Navier–Stokes solver for the simulation of collapsing cavitation bubbles near to elastic surfaces of solids. *Ph.D. Thesis*, RWTH Aachen, 1997, Shaker–Verlag (in German).
26. Welch J, Harlow F, Shannon J, Daly B. The MAC method—a computing technique for solving viscous incompressible transient fluid-flow problems involving free surfaces. *Technical Report*, Los Alamos Scientific Laboratory of the University of California, 2000.
27. Hirt C, Nichols B. VOF method for the dynamics of free boundaries. *Journal of Computational Physics* 1979; **39**:201–225.

DOI: 10.1002/fld

28. Brackbill JU, Kothe DB, Zemach C. A continuum method for modeling surface tension. *Journal of Computational Physics* 1992; **100**:335–354.
29. Osher S, Fedkiw RP. Level set methods: an overview and some recent results. *Journal of Computational Physics* 2001; **169**:463–502.
30. Sethian JA. *Level Set Methods*. Cambridge Monographs on Applied and Computational Mathematics. Cambridge University Press: Cambridge, 1996.
31. Sussman M, Smereka P, Osher S. A level set approach for computing solutions to incompressible two-phase flows. *Journal of Computational Physics* 1994; **114**:146–159.
32. Sussman M, Almgren AS, Bell JB, Colella P, Howell LH, Welcome ML. An adaptive level set approach for incompressible two-phase flows. *Journal of Computational Physics* 1999; **148**:81–124.
33. Abgrall R. Generalisation of the Roe scheme for the computation of mixture of perfect gases. *Journal of Computational Physics* 1996; **125**:150–160.
34. Fedkiw RP, Aslam T, Merriman B, Osher S. A non-oscillatory Eulerian approach to interfaces in multimaterial flows (the ghost fluid method). *Journal of Computational Physics* 1999; **152**(2):457–492.
35. Fedkiw RP, Aslam T, Xu S. The ghost fluid method for deflagration and detonation discontinuities. *Journal of Computational Physics* 1999; **154**:393–427.
36. Abgrall R, Karni S. Ghost-fluids for the poor: a single fluid algorithm for multifluids. In *Hyperbolic Problems*: *Theory*, *Numerics*, *Applications*, Freistühler H, Warnecke G (eds). Birkhäuser Verlag: Basel, 2001; 1–10.
37. Sussman M. A second order coupled level set and volume-of-fluid method for computing growth and collapse of vapor bubbles. *Journal of Computational Physics* 2003; **187**:110–136.
38. Andreae S, Ballmann J, Müller S. Wave processes at interfaces. In *Analysis and Numerics for Conservation Laws*, Warnecke G (ed.). Springer: Berlin, 2005; 1–25.
39. Andreae S. Wave interactions with material interfaces. *Ph.D. Thesis*, RWTH Aachen, 2007.
40. Harten A. Adaptive multiresolution schemes for shock computations. *Journal of Computational Physics* 1994; **115**:319–338.
41. Harten A. Multiresolution algorithms for the numerical solution of hyperbolic conservation laws. *Communications on Pure and Applied Mathematics* 1995; **48**(12):1305–1342.
42. Müller S. *Adaptive Multiscale Schemes for Conservation Laws*. Lecture Notes in Computational Science and Engineering, vol. 27. Springer: Berlin, 2002.
43. Cohen A, Kaber SM, Müller S, Postel M. Fully adaptive multiresolution finite volume schemes for conservation laws. *Mathematics of Computation* 2003; **72**:183–225.
44. Bramkamp F, Lamby Ph, Müller S. An adaptive multiscale finite volume solver for unsteady and steady state flow computations. *Journal of Computational Physics* 2004; **197**(2):460–490.
45. lau Cohen A, Kaber SM, Postel M. Multiresolution analysis on triangles: application to gas dynamics. In *Hyperbolic Problems*: *Theory*, *Numerics*, *Applications*, Freistühler H, Warnecke G (eds). Birkhäuser Verlag: Basel, 2001; 257–266.
46. Roussel O, Schneider K. A fully adaptive multiresolution scheme for 3D reaction–diffusion equations. In *Finite Volumes for Complex Applications*, Herbin B (ed.). Hermes Science: Paris, 2002.
47. Roussel O, Schneider K, Tsigulin A, Bockhorn H. A conservative fully adaptive multiresolution algorithm for parabolic PDEs. *Journal of Computational Physics* 2003; **188**(2):493–523.
48. Müller S, Stiriba Y. Fully adaptive multiscale schemes for conservation laws employing locally varying time stepping. *Journal of Scientific Computing* 2007; **30**(3):493–531.
49. Lamby Ph, Müller S, Stiriba Y. Solution of shallow water equations using fully adaptive multiscale schemes. *International Journal for Numerical Methods in Fluids* 2005; **49**(4):417–437.
50. Lamby Ph, Massjung R, Müller S, Stiriba Y. Inviscid flow on moving grids with multiscale space and time adaptivity. In *Proceedings of Enumath 2005 the 6th European Conference on Numerical Mathematics and Advanced Mathematics*, Bermudez de Castro A, Gomez D, Quintela P, Salgado P (eds). Numerical Mathematics and Advanced Applications. Springer: Berlin, 2006; 755–764.
51. Guderley G. Starke kugelige und zylindrische Verdichtungsstöße in der Nähe des Kugelmittelpunktes bzw. der Zylinderachse. *Luftfahrtforschung* 1942; **19**:302–312.
52. Popinet S, Zaleski S. Bubble collapse near a solid boundary: a numerical study of the influence of viscosity. *Journal of Fluid Mechanics* 2002; **464**:137–163.
53. Cocchi JP, Saurel R, Loraud JC. A Riemann problem based method for the resolution of compressible multimaterial flows. *Journal of Computational Physics* 1997; **137**(2):265–298.
54. Barberon Th, Helluy Ph, Rouy S. Practical computation of axisymmetrical multifluid flows. *International Journal of Finite Volumes* 2003; **1**(1):1–34.

DOI: 10.1002/fld

55. Gallouët T, Hérard JM, Seguin N. A hybrid scheme to compute contact discontinuities in one-dimensional Euler systems. *M2AN Mathematical Modelling and Numerical Analysis* 2003; **36**(6):1133–1159.
56. Barberon Th, Helluy Ph. Finite volume simulation of cavitating flows. *Computers and Fluids* 2005; **34**(7):832–858.
57. Karni S. Multicomponent flow calculations by a consistent primitive algorithm. *Journal of Computational Physics* 1994; **112**(1):31–43.
58. Abgrall R. Generalisation of the Roe scheme for the computation of mixture of perfect gases. *Recherche Aérospatiale* 1988; **6**:31–43.
59. Wackers J, Koren B. A fully conservative model for compressible two-fluid flow. *International Journal for Numerical Methods in Fluids* 2005; **47**(10–11):1337–1343.
60. Colella Ph, Glaz HM. Efficient solution algorithms for the Riemann problem for real gases. *Journal of Computational Physics* 1985; **59**:264–289.
61. Müller S. Extension of ENO-procedures to two space dimensions and application to hypersonic stagnation point problem. *Ph.D. Thesis*, RWTH Aachen, 1993 (in German).
62. Harten A, Engquist B, Osher S, Chakravarthy SR. Uniformly high order accurate essentially non–oscillatory schemes III. *Journal of Computational Physics* 1987; **71**:231–303.
63. Barberon Th. Modélisation mathématique et numérique de la cavitation dans les écoulements multiphasiques compressibles. *Ph.D. Thesis*, Université de Toulon et du Var, 2002.
64. Arandiga F, Donat R, Harten A. Multiresolution based on weighted averages of the hat function I: linear reconstruction techniques. *SIAM Journal on Numerical Analysis* 1998; **36**(1):160–203.
65. Carnicer JM, Dahmen W, Peña JM. Local decomposition of refinable spaces and wavelets. *Applied and Computational Harmonic Analysis* 1996; **3**:127–153.
66. Osher S, Sanders R. Numerical approximations to nonlinear conservation laws with locally varying time and space grids. *Mathematics of Computation* 1983; **41**:321–336.
67. Berger MJ, Oliger J. Adaptive mesh refinement for hyperbolic partial differential equations. *Journal of Computational Physics* 1984; **53**:484–512.
68. Berger MJ, LeVeque RJ. Adaptive mesh refinement using wave-propagation algorithms for hyperbolic systems. *SIAM Journal on Numerical Analysis* 1998; **35**(6):2298–2316.
69. Dickopp Ch, Ballmann J. Two-phase flow through injection nozzles. In *Hyperbolic Problems*: *Theory*, *Numerics*, *Applications*, Asakura F, Aiso H, Kawashima S, Matsumura A, Nishibata S, Nishihara K (eds). Yokohama Publishers: Japan, 2006; 351–358.
70. Saurel R, Cocchi JP, Butler PB. A numerical study of cavitation in the wake of a hypervelocity underwater projectile. *AIAA Journal of Propulsion and Power* 1999; **15**(4):513–522.
71. Henderson LF. On shock impedance. *Journal of Fluid Mechanics* 1970; **40**:719–735.
72. Thompson PA. *Compressible Fluid Dynamics*. McGraw-Hill: New York, 1972.
73. Cocchi JP, Saurel R, Loraud JC. Treatment of interface problems with Godunov-type schemes. *Shock Waves* 1996; **5**:347–357.
74. Specht U. Numerical simulation of mechanical waves at fluid–solid-interfaces. *Ph.D. Thesis*, RWTH Aachen, 2000; VDI–Verlag, Reihe 7 (in German).
75. Nourgaliev RR, Dinh TN, Theofanous TG. Adaptive characteristics-based matching for compressible multifluid dynamics. *Journal of Computational Physics* 2006; **213**:500–529.

DOI: 10.1002/fld